Producing Synthetic Maps Of Dust Polarization Using A Velocity Channel Gradient Technique

by

Zekun Lu

A thesis submitted in partial fulfillment of the requirements for the degree of

Master of Science

Department of Physics
University of Alberta

Abstract

In modern cosmology, many efforts have been put to detect primordial B-mode of cosmic microwave background polarization from the gravitational waves generated during inflation. Considering the foreground dust contamination of microwave polarization maps, it is essential to obtain a precise prediction for polarization in dust emission. In this work, we show a new method to produce synthetic maps of dust polarization in magnetized turbulent interstellar medium from more abundant high-resolution HI data. By using Velocity Channel Gradient technique, we are able to predict both direction and degree of dust polarization by investigating spectroscopic HI information in position-position-velocity space. We apply our approach to The Galactic Arecibo L-band Feed Array HI data, and find a good correspondence between synthesized maps and Planck's polarization measurements at 353 GHz. We also discuss how to incorporate noise information into the VChG method. Our method also provides a way to study Galactic magnetic fields from abundant HI data without reliance on true polarization mapping.

Preface

This thesis is original work by Zekun Lu under the supervision of Prof. Dmitri Pogosyan. The main results of this thesis have been published in Lu et al. (2020) in collaboration with Prof. Alex Lazarian and Prof. Dmitri Pogosyan. Chapters 3, 4, 5 closely follow the publication while Chapters 1, 2, 6, 7 are expanded and rewritten. In the publication Lu et al. (2020), I wrote the code pipeline of VChG method, analyzed numerical simulation, reduced and analyzed the GALFA-HI and Planck data and wrote major portion of the paper. The analytical analysis was done in collaboration with Prof. Dmitri Pogosyan. Prof. Alex Lazarian provided overall guidance on gradient method and MHD turbulence theory. The simulation data in Chapter 4 are provided by Prof. Alex Lazarian. Generation of MHD mode realizations in Chapter 6 uses the code by Prof. Dmitri Pogosyan. All observational data used are publicly available.

Acknowledgements

Contents

List of Tables

List of Figures

List of Abbreviations

CMB	Cosmic microwave bacground
FWHM	Full width at half maximum
GALFA-HI	Galactic Arecibo L-band Feed Array HI
IGW	Inflationary gravitational wave
ISM	Interstellar medium
LOS	Line-of-sight
MHD	Magnetohydrodynamic
PPP	Position-position-position
PPV	Position-position-velocity
RAT	Radiative torque
RHT	Rolling Hough Transform
VChG	Velocity Channel Gradient
VGT	Velocity Gradient Technique

Chapter 1

Introduction

"Where are we from" is one of the most basic philosophical questions that we humans want to answer. Such question can be approached from different scales, for example, the origin and evolution of planet, star, galaxy and ... the most mysteriously, the Universe. Since the last century (Hartmann 1904, Trumpler 1930), astronomers realized that we live in a Galaxy filled with interstellar medium (ISM), the matter among stars, which mostly exists as gas and dust. Such medium is the fuel and cradle of new stars, but paradoxically, also the veil that has to be lifted if we want to see the clear face of the outside universe.

1.1 The primordial gravitational wave from inflation

The current hot Big Bang model postulates that the universe experienced an ephemeral but intense (nearly exponential) expansion in its early era, which is called as the inflation era. Consequently, two types of perturbations were produced during such process, scalar perturbations (density waves) and tensor perturbations (gravitational waves, hence GWs). The primordial density waves, as the sculptor of the cosmic microwave background radiation (CMB),

The Gravitational Wave Spectrum
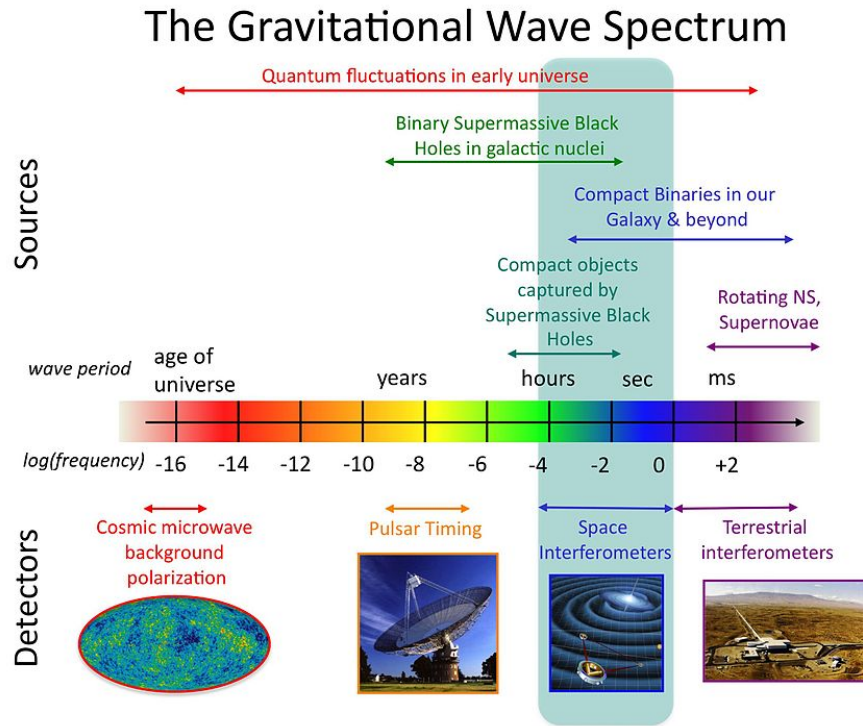
Figure 1.1: The Gravitational wave spectrum with marked different sources and detectors. Credit: NASA Goddard Space Flight Center.

can be directly detected by the anisotropy of the CMB temperature field (Hu & Dodelson, 2002). However, the detection of the inflationary GWs (IGWs, also called the primordial GWs) is more difficult and is the missing piece of the jigsaw puzzle for cosmologists. Note that, with the knowledge of scalar perturbations, the level of the tensor perturbations are usually expressed as the tensor-to-scalar ratio, r, which is defined as the ratio between amplitude of the gravitational wave and the density wave. The most recent constraint from *Planck* on the tensor-to-scalar ratio is $r < 0.10$ (Planck Collaboration et al., 2020).

Encouraged by recent a series of detections of GWs by LIGO (Laser Interferometer Gravitational-Wave Observatory) and Virgo collaborations (Abbott et al. 2016a, 2016b, 2017b, 2017c for black hole GWs; Abbott et al. 2017d for
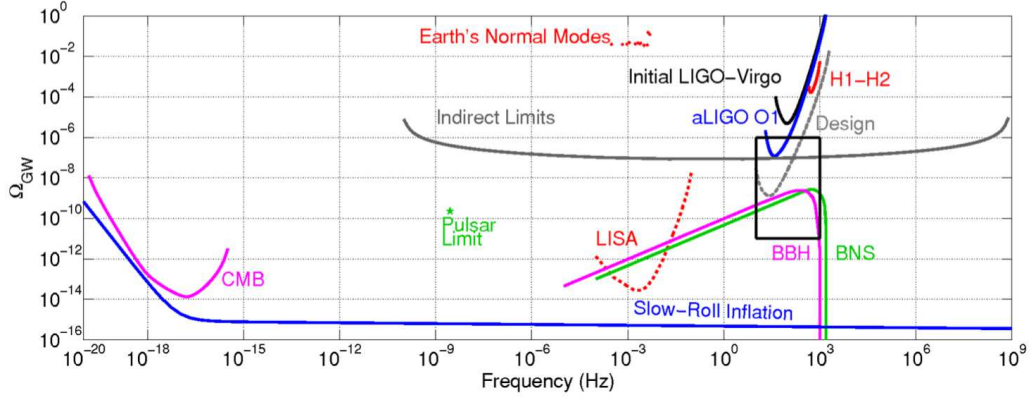
Figure 1.2: The expected energy density of background gravitational wave in slow-roll inflationary models (blue curve) versus energy sensitivity limits of current and future GW detectors. Direct GW detectors (e.g LIGO in grey, LISA in dotted red) are designed to work at frequencies $10^{-5}-10^3$ Hz where the IGW power is strongly suppressed and the main GW signals come from neutron stars (BNS) or black hole (BBH) mergers. In contrast, CMB experiments can indirectly detect IGW at $10^{-20} - 10^{-18}$ Hz frequencies. Credit: Abbott et al. (2017a).

neutron star GWs; and references subsequently), it is natural to ask whether it is possible to directly detect the IGWs. To answer the question, we need to first know the spectrum of GWs from different sources. As shown in Figure 1.1, the GWs with astrophysical sources are located in the high-frequency side of the spectrum ($\gtrsim 10^{-9}$ Hz), which is also the frequency range that current detectors are able to reach. Meanwhile, we can see that the GWs from the early universe are omnipresent, spanning from the low-frequency end to the high-frequency end at the spectrum which kindles the hope to directly detect the IGWs. Nevertheless, when evaluating the performance of detectors, besides the temporal resolution, the energy sensitivity also counts. By viewing the Figure 1.2, we can see that the GW energy density Ω_{GW} of IGW plummets when the frequency gets larger and then stays at a very low level ($\sim 10^{-15}$), which is much lower than the sensitivity of current detectors (for example, the maximal designed sensitivity of LIGO and VIRGO is $\sim 10^{-9}$). A possible window for energy sensitivity is at very low frequency ($\lesssim 10^{-15}$ Hz), where we can see a bump

3

of IGW's energy density, while such frequency is too low for current detectors ($\gtrsim 10^{-9}$ Hz). Therefore, as the answer to our natural question, at least in foreseeable near future, it is impossible to directly detect the IGW. Resorting to an alternative method to hunt the IGW becomes necessary.

1.2 The CMB and its polarization

Fortunately, during later evolution of the universe, the IGWs left some unique polarization, which makes it possible to indirectly detect the IGW if we could catch such unique polarized imprints.

In more detail, at the end of inflation, the universe has reheated to continue expansion from a hot state in thermal equilibrium as in standard Big Bang cosmology (the evolution history of the universe can be found in any modern cosmology textbook, e.g. Ryden 2016). As the Universe cooled down due to expansion to temperatures below 1 GeV, its particle content reduced to that of protons and neutrons (baryons) as well as electrons and positrons and neutrinos. As the universe further expanded, at $T \sim 0.1$ MeV it passes through a brief period of nucleosynthesis when the light elements (predominantly helium) are formed from hydrogen (protons) and free neutrons. The temperature of the soup was still high so that the ionized matter in the plasma were tightly coupled to photons. The mean free path of photons due to Thomson scattering on electrons was very short and the universe was highly opaque. Then as the temperature decreases to 10 eV range, we enter the epoch of formation of the Cosmic Microwave Background (CMB). Three time events are worth mentioning there. First, as the universe continued to cool, the electrons and protons would tend to combine with each other and become neutral (actually there was also helium but mostly hydrogen). At the moment when the number density of ions equaled to that of neutral atoms, the universe reached the epoch of *recombination* (Temperature $T \sim 3700$ K; age of universe ~ 0.25 Myr; Kolb

& Turner 1990). With fewer free electrons, the scattering rate between photons and electrons would decrease correspondingly. Second, when the rate of photons' Thomson scattering became smaller than the rate of universe's expansion, the universe reached the epoch *of photon decoupling* ($T \sim 3000 \ K$, age $\sim 0.37 \ Myr$, Planck Collaboration et al. 2016e), since then the universe became transparent. Shortly thereafter when the last photon scattered with electron, the universe reached the epoch *of last scattering*, since when the photons would move completely freely until they meet us, the observers (fine distinction between the moment of the photon decoupling and last-scattering is that the last-scattering occurs at different moment along different LOS, so the surface of last scattering is rugged). Note that although we call background radiation as CMB, at the last scattering surface, such radiation was not in microwave wavelength, but in visible/ near infrared wavelength, which was later constantly stretched by the universe expansion and finally received as microwave radiation by current observers. More importantly, the CMB radiation is a black-body radiation to very high precision, which means the energy spectrum of CMB radiation solely depends on the temperature.

As the oldest light that we could receive, the CMB carries substantial information about the early universe. Penzias & Wilson (1965) first successfully discovered the CMB, the relic of the young, hot and dense universe, which provided a solid support for the hot Big Bang theory and won the 1978 Nobel Prize in Physics. Inspired by the landmark discovery, more projects were conducted to observe more details of the CMB. As a huge success, recognized by the Nobel Prize in Physics 2006, the Cosmic Microwave Background Explorer (COBE) satellite (Smoot et al., 1992) discovered the slight anisotropy of the CMB radiation temperature, which brought the CMB studies to a new precise era. Later at the turn of the century, two competing balloon-based experiments Balloon Observations Of Millimetric Extragalactic Radiation ANd Geophysics (BOOMERanG; de Bernardis et al. 2000) and Millimeter Anisotropy eXperi-

ment IMaging Array (MAXIMA; Balbi et al. 2001) determined the geometry of the universe to be almost flat, by observing the CMB in a small sky region. More recently, NASA and ESA consecutively launched full-sky multi-frequency space CMB missions The Wilkinson Microwave Anisotropy Probe (WMAP; Bennett et al. 2003) and Planck (Planck Collaboration et al. 2011a), which provided the most precise determination of cosmological parameters to date.

In addition to the temperature information, more secrets can be dug out if the polarization of CMB can be observed. We know that the CMB photons were scattered by electrons through Thomson scattering, during which process the incident photon accelerates the electron and the accelerated electron will in turn re-radiate the photon with the same frequency. The scattered CMB photons are polarized along the motion of accelerated electrons. Naturally, if the incident CMB photons are isotropic, coming from all the direction with equal intensity, the scattered CMB photons will be unpolarized. However, as mentioned in section 1.1, the inflation of the early universe was postulated to produce scalar perturbations and tensor perturbations, both of which could generate a quadrupole anisotropic temperature field. Since the CMB radiation is black-body radiation, anisotropic temperature variations induce anisotropic energy variations. Therefore, with the partially quadrupole-anisotropic incident photons, the scattered CMB photons were partially linear polarized.

However, the quadrupole anisotropy caused by the two types of perturbations are different. Briefly speaking, the quadrupole anisotropy produced by the scalar perturbations (density waves) is azimuthally symmetric, whereas the quadrupole produced by the tensor perturbations (gravitational waves) is asymmetric. Consequently, after the Thomson scattering, density waves generate both E-mode (like electronic field) and B-mode polarization (like magnetic field) while gravitational waves generate only B-mode polarization. Power spectra of the CMB from density waves (left) and gravitational waves (right) are shown in Figure 1.3. It is necessary to clarify that the B-mode power spectrum
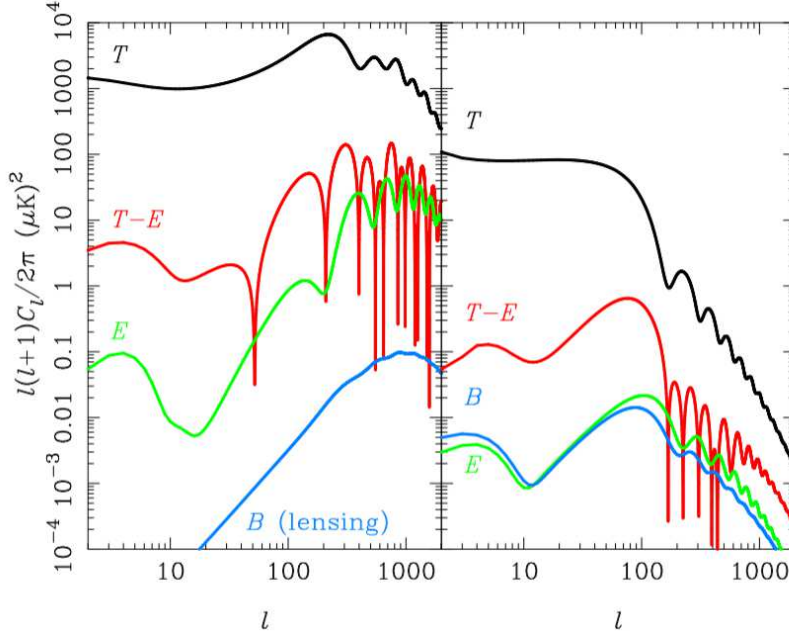
Figure 1.3: Predicted angular power spectra of the CMB as functions of spherical multipole l from density waves (left) and gravitational waves (right), where different colors mark different fields (temperature in black, E-mode in green, T-E cross-correlation in red and B-mode in blue). The power spectrum of B-mode from weak gravitational lensing is marked in brackets. Credit: Challinor & Peiris (2009).

shown in the scalar perturbation is produced by weak gravitational lensing, a statistically determined space bending effect by usually clusters of galaxies, not from the aforementioned inflationary scalar perturbations. Such a lensing B-mode was first detected by South Pole Telescope (SPT; Hanson et al. 2013). Perplexing as it seems, the lensing B-mode prevails in small scales (spherical multipole $l > 100$), whereas the power spectrum of B-mode polarization from IGWs peaks at $l \sim 100$ and remains evident at larger scale ($l < 100$), which makes the two B-modes distinguishable. Therefore, in large scale, the uniqueness of the B-mode polarization can be used to indirectly hunt the gravitational waves from the early inflation era, IGWs.

As one of the twin polarizations, the CMB E-mode was first detected by the Degree Angular Scale Interferometer (DASI; Kovac et al. 2002) and further
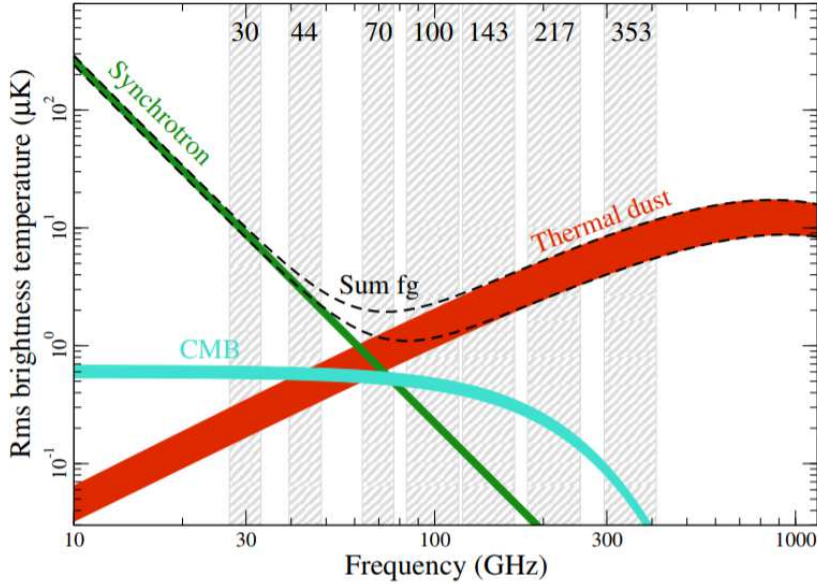
Figure 1.4: The brightness temperature of the foreground and CMB polarizations in different frequencies. Credit: Planck Collaboration et al. (2016c).

refined by followed experiments, e.g. WMAP (Page et al., 2007), the Cosmic Anisotropy Polarization Mapper (CAPMAP; Bischoff et al. 2008), Background Imaging of Cosmic Extragalactic Polarization1 (BICEP1; Barkats et al. 2014), which provided a strong support for the theoretical framework constructed by CMB temperature observations, but still not definitive to break the degeneracy of the paradigms for the early universe. Detection of the CMB B-mode polarization would be a critical strike.

1.3 Why is foreground polarization important?

The BICEP2 Collaboration (Ade et al., 2014) was the first group that claimed the detection of CMB B-mode polarization from the IGW, with the tensor-to-scalar ratio $r = 0.20^{+0.07}_{-0.05}$, excluding the null hypothesis at $> 5\sigma$ significance. However, the later joint analysis of BICEP2/*Keck Array* and *Planck* data (Ade et al., 2015) found that such excess of B-mode polarization signal could be interpreted as the contribution of Galactic dust emission and constrain the r

value by an upper limit $r < 0.12$ at 95% confidence, which provided a startling illustration of the importance of careful analysis of the foregrounds for cosmological B-mode detection.

As shown in Figure 1.4, two important sources of foreground polarization are synchrotron polarization and thermal dust polarization (see Ichiki 2014 for a review). The synchrotron polarization, arising from the interactions between cosmic ray electrons and interstellar magnetic fields, dominates at low microwave frequencies ($\lesssim 30$ GHz). The thermal dust polarization, arising from the aspherical interstellar dust grains (will be introduced in more details at section 2.2), dominates at higher frequencies ($\gtrsim 70$ GHz). By revisiting the Figure 1.4, we can see that the brightness temperature of those foreground polarized signals are larger than the CMB polarized signals, thus swallowing the distant cosmological polarization. Therefore, it is prerequisite to obtain a precise foreground polarization before we are able to separate and detect the CMB B-mode polarization. Reconstructing the synchrotron polarization using the synchrotron gradient technique was studied by Lazarian et al. 2017 and Lazarian & Yuen 2018b. In this thesis, I focus on reconstruction of the thermal dust polarization.

In practice, the foreground polarizations are not easily subtracted. Taking Planck experiment as an example, what the telescope has observed are seven frequency maps from 30 GHz to 353 GHz. Different foreground components as well as CMB signal are then separated by combining and interpolating the multi-frequency maps following certain pipelines (Planck Collaboration et al. 2016a,b,d), where in particular the frequency map at 353 GHz is dominated by thermal dust polarization and provides much information on the dust foreground (Planck Collaboration et al., 2015). Moreover, the raw CMB polarization signal in *Planck* measurements has low signal to noise ratio even for E-mode of polarization, the situation which will persist for B-mode for upcoming experiments as well. Thus, it is important to look for any additional

alternative methods (like the HI method to be described in section 1.5) to produce extra independent foreground polarization templates that can be included in better foreground subtraction.

It is necessary to point out that, although all the aforementioned story unfolds around IGW and CMB, the foreground polarization is also of interest and essential for the study of interstellar magnetic field, whose importance can be reflected in two aspects. First, pervading the ISM, the interstellar magnetic field plays an important role in a series of astrophysical processes, e.g. cosmic ray propagation (Jokipii, 1966) and star formation (McKee & Ostriker, 2007). Hence a precise measurement is a necessity to understand these processes. Second, important as it is, the interstellar magnetic field is notoriously difficult to measure (Haverkorn, 2015), where, so far, only limited methods are available in our toolbox to measure interstellar magnetic fields and certain method only applies to certain ISM phase, obtaining certain component of magnetic fields (Han, 2017). The line-of-sight component of magnetic field strength can be measured by the Zeeman splitting and Faraday rotation of linear polarization, where the Zeeman splitting method works in the cold neutral medium (Heiles & Troland, 2005) and dense molecular clouds (Crutcher, 1999) while the Faraday rotation method works in ionized medium (Noutsos, 2012). The plane-of-sky component of magnetic field can be measured by the foreground polarization, i.e. synchrotron, thermal dust and starlight polarization (the starlight itself is not polarized but a result of dust extinction). More exactly, the synchrotron and thermal dust polarization are polarized perpendicular to the interstellar magnetic field while the starlight polarization aligns the interstellar magnetic field, which is why the polarimetry is widely used as a probe of magnetic fields (Haverkorn, 2015). The starlight and thermal dust polarizations are both results of alignment of the aspherical dust grains, which is further explained in section 2.2.

1.4 HI and the 21-cm line

The ISM mainly consists of gas and dust, together with cosmic rays, electromagnetic radiation, interstellar magnetic field, the gravitational field and the dark matter (the overview can be found in Draine 2011). Persisting since the epoch of *recombination*, the interstellar gas primarily consists of hydrogen (mass fraction $\sim 73\%$) and helium (mass fraction $\sim 27\%$), where the hydrogen consists of different phases, with mass fraction $\sim 23\%$ HII (ionized hydrogen), $\sim 60\%$ HI (neutral hydrogen) and $\sim 17\%$ H_2 (molecular hydrogen). Atomic HI, as a pervasive medium, is an excellent probe of the Galactic structure thorough 21-cm line, the focus of this thesis.

The 21-cm line is formed by the energy transition between the hyperfine-split energy states of the hydrogen atom ground state (a detailed derivation can be found in Bradt 2014). Both proton and electron have intrinsic magnetic dipole moments, which are aligned with their spins. The electron, in addition, has a dipole magnetic moment associated with the orbital angular momentum. In HI atom, magnetic interaction between electron and proton dipoles lead to their alignment, and, therefore, in the ground state where the orbital momentum is zero, to the alignment of their spins. As a result, the spin angular momentum of electron is either parallel or antiparallel to that of proton, leading to two energy states, with $\sim 5.9 \times 10^{-6}$ eV energy difference. Thus, transition (absorption or emission) between the hyperfine states produces the 21-cm line, which, first detected by Ewen & Purcell (1951), opens a vital radio window for galaxy studies. One advantage of 21-cm hydrogen line is that this radio signal is hardly scattered except in very dense regions, so that we could look deep into the ISM along the line of sight (LOS), and measure its LOS velocity via the line Doppler shift.

Revealed by a series of HI surveys, e.g. Leiden-Dwingeloo survey (LDS; Hartmann & Burton 1997), the Canadian Galactic Plane Survey (CGPS; Taylor
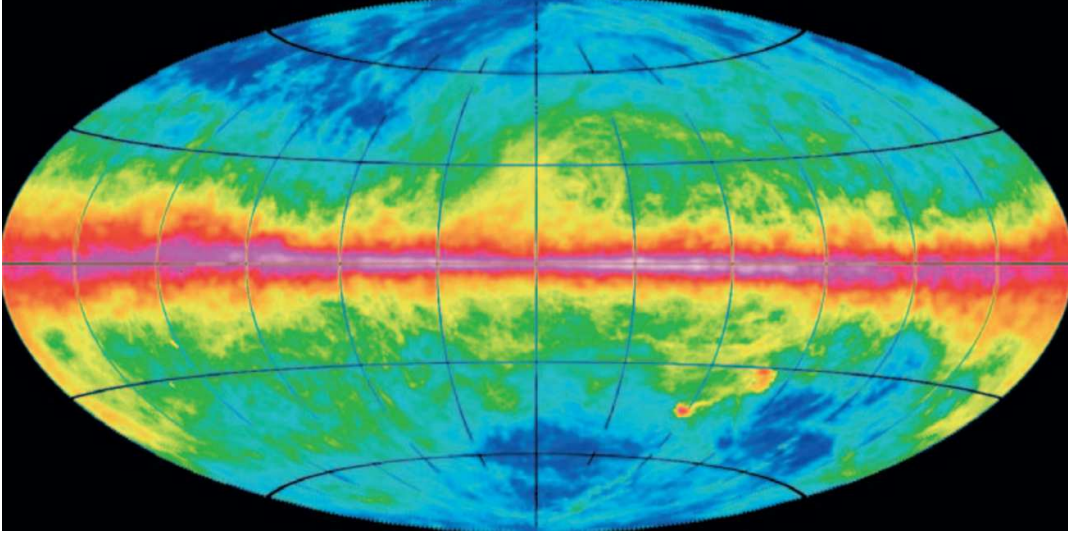
Figure 1.5: The integrated full-sky HI emission over the velocity range -400< v <+400 km s^{-1} observed by the Leiden/Argentine/Bonn survey (LAB; Kalberla et al. 2005).

et al. 2003), the Leiden/Argentine/Bonn survey (LAB; Kalberla et al. 2005) and the Parkes Galactic All-Sky Survey (GASS; McClure-Griffiths et al. 2009), a highly complex picture of the Galactic HI was summarized poetically as "a violent, breathing disk surrounded by highly turbulent extra-planar gas" in Kalberla & Kerp (2009).

A view of full-sky HI emission by the LAB is shown in Figure 1.5. In this thesis, we mainly pay attention to the anisotropic structures of the high galactic latitude HI. When we observe in the direction of high galactic latitudes, we look through several hundred parsecs of turbulent atomic gas moving with relative LOS velocities reaching $\sim 10 - 15$ km/s. Phases and dynamics of HI will be investigated later in section 2.1.

Several full-sky and specific HI surveys are ongoing or planned for the future, e.g. the HI4PI survey HI4PI Collaboration et al. 2016, the Galactic Arecibo L-band Feed Array HI (GALFA-HI; Peek et al. 2018), the Five-hundred-meter Aperture Spherical Telescope HI survey (FAST; Zhang et al. 2019), An Square Kilometre Array Pathfinder HI All-Sky Survey (WALLABY; Koribalski et al.

2020), with higher sensitivity or higher spacial resolution, which makes the Galactic HI data abundant and easily available. Therefore, it would be a convenient and powerful technique if the HI can be used as an independent technique to probe the Galactic magnetic field and dust polarization.

1.5   Using HI to predict dust polarization

The HI is correlated with dust, in the sense of both intensity and polarization.

By analyzing the first full-sky dust emission data at 60 μm and 100 μm from the Infrared Astronomical Satellite (IRAS), Boulanger & Perault (1988) found a tight correlation between infrared dust emission and HI 21-cm emission at high Galactic latitude, which was a decade later extended to the far-infrared wavelength (Boulanger et al., 1996) by investigating the dust emission data from the COBE, as shown in Figure 1.6. Reprocessing the composite of IRAS/ COBE dust maps, Schlegel et al. (1998) further confirmed the dust-HI emission correlation. Nevertheless, question remains that in what spacial scale and physical phase HI correlates with dust (Kalberla et al., 2016).

More recently, Planck released the full-sky complete Stokes-parameters maps of thermal dust at 353 GHz (Planck Collaboration et al., 2015), which is up to date the most sensitive and high-resolution full-sky dust map, with both intensity and polarization information. Using the GALFA-HI survey and comparing with Planck 353 GHz, Clark et al. (2015) noticed that HI filaments are aligned with interstellar thermal dust polarization/ magnetic field at high Galactic latitude, which was proposed as an independent method to trace magnetic fields and constrain Galactic foregrounds. Later in (Clark 2018), such method was developed to predict degree of polarization. Extracting filaments structures from the GASS III full-sky HI map (Kalberla & Haud, 2015) and comparing with the Planck 353 GHz map, Kalberla et al. (2016), as shown in Figure 1.7, found that the HI filaments well correlate with both dust emission and po-
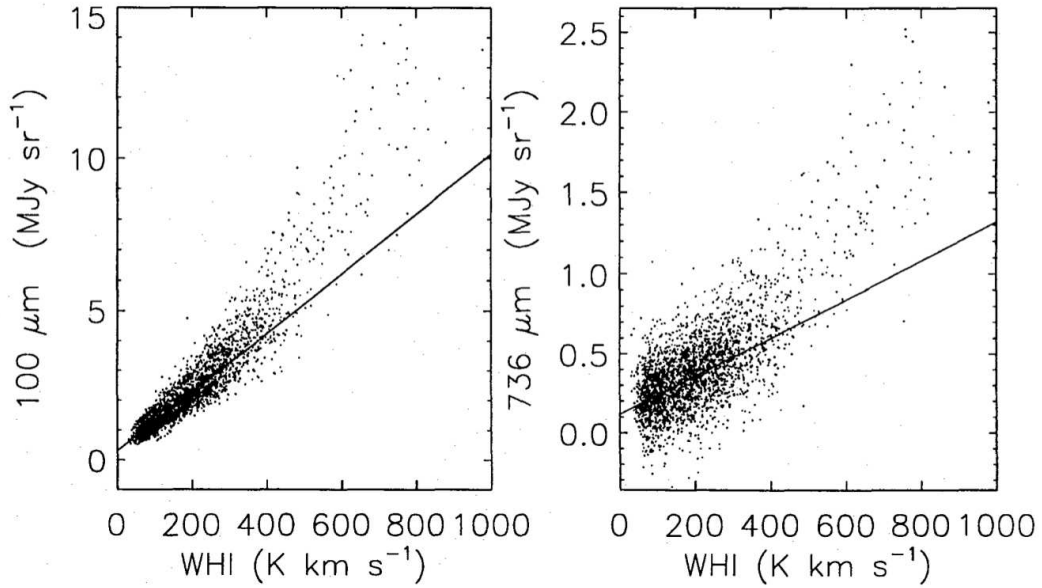
Figure 1.6: The correlation between infrared (IR) dust emission and HI 21-cm emission. The left panel shows the IR dust emission at 100 μm from the Diffuse Infrared Background Experiment (DIRBE). The right panel shows the IR dust emission at 736 μm from the Far-Infrared Absolute Spectrophotometer (FIRAS), which is averaged between 600 and 900 μm. Both IR instruments are on board the Cosmic Background Explorer (COBE). The HI 21-cm emission is from the Leiden/ Dwingeloo survey. Note that the linear line only fits the data at $W_{HI} < 250$ K km s^{-1}. Credit: Boulanger et al. (1996).

larization, where HI shows even more substructures than dust emission. This supports that HI could work independently to trace the dust polarization/ magnetic fields, even promisingly with higher precision than polarimetry at the high Galactic latitude regions. Moreover, using the constraints of distance ~ 100 pc (Lallement et al., 2014) and magnetic field strength $B_{tot} = (6.0 \pm 1.8)\ \mu G$ (Heiles & Troland, 2005), the authors estimates the median volume density of the HI filaments to be $14 \lesssim n \lesssim 47$ cm^{-3}, which indicates that the HI filaments mainly exist in the cold neutral medium (CNM) phase, embedded in outer warm neutral medium (WNM).

In parallel to this direction suggested by S. Clark and her collaborators on the basis of observational studies, a theory-based approach was developed by the Lazarian's research group (see González-Casanova & Lazarian 2017, Yuen & Lazarian 2017, Lazarian & Yuen 2018a, Lazarian et al. 2018, Hu et al. 2018). This approach of tracing interstellar magnetic field is based on the property of velocity gradients to be aligned perpendicular to magnetic field in MHD turbulence. The interstellar medium, including HI gas, is known to be turbulent (Larson 1981, Armstrong et al. 1995, Lazarian & Pogosyan 2000, Stanimirović & Lazarian 2001, McKee & Ostriker 2007, Lazarian 2009, Chepurnov & Lazarian 2010, Xu & Zhang 2016a, 2016b). This justifies the application of the Velocity Gradient Technique (VGT) to HI.

Among the modifications of the technique, the Velocity Channel Gradients (VChGs) technique described in Lazarian & Yuen (2018a) was shown the most promising. The technique makes use of the theory of non-linear mapping of turbulent motions from the Position-Position-Position (PPP) space into the Position-Position-Velocity (PPV) space developed in Lazarian & Pogosyan (2000, 2004).

While the technique proposed by Clark et al. (2015) was from the very beginning aimed at obtaining the information that can be used to study foreground polarization, the VChGs were used mostly for magnetic field studies,
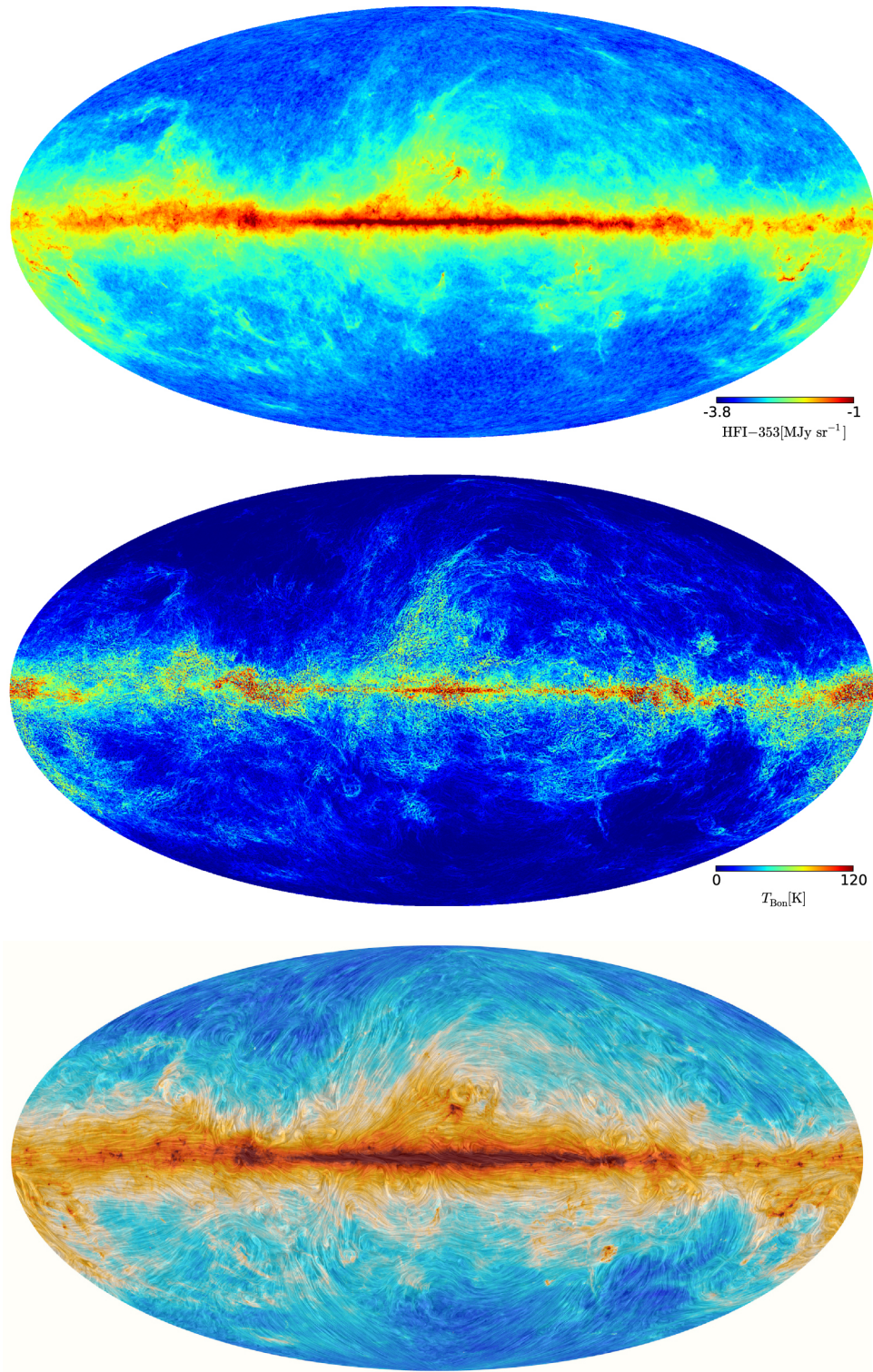
Figure 1.7: Comparisons between HI 21-cm map and dust emission/ polarization. Top panel: Planck 353 GHz map. Middle panel: brightness temperature map of HI filaments. Bottom panel: thermal dust polarization map. Credit: Kalberla et al. (2016).

in particular, for magnetic field studies in molecular clouds (Hu et al., 2019a). The studies of magnetic field in HI were also performed, but they were aimed at studies of magnetic fields and magnetization of media (Lazarian & Yuen 2018a, Lazarian et al. 2018) rather than on the CMB foreground studies. In this thesis we explore the latter application of the VChGs.

In spite of the progress that we have made, as a pioneering method, the VChG can be improved from two aspects. For one thing, in the original idea of VChG, the description of polarization is incomplete, which only includes the direction but lack the degree of polarization. In this thesis, we improve this by constructing pseudo Stokes parameters, making it possible to estimate degree of polarization. For another, as for the statistical distribution of local gradient angles, the previous method gives a phenomenological fitting but lacks a theoretical/mathematical understanding. We advance analytical statistical study of the local distribution of gradient angles, which helps us further understand the behaviour of VChG, for example, taking the HI noise into consideration and also potentially relate the observations to particular models of the turbulence.

1.6   Structure of thesis

The structure of the thesis is as follows. Chapter 2 introduces the theoretical considerations for the VChG method, i.e. why HI morphology and dust polarization connect with interstellar magnetic fields, as well as why the gradient method tracks the magnetic field statistically. Chapter 3 describes the methodology and pipeline of the VChG method. Chapter 4 presents the numerical tests of the VChG in different magnetization. Chapter 5 provides a comparison between the synthetic dust polarization maps from GALFA-HI data and the thermal dust polarization at 353 GHz map from Planck. In chapter 6, I discuss the limitations and applicability of the VChG. Moreover, I evaluate quantitatively the influence of observational noise and the result of noise cor-

rection, which would be a direction for my future work. Finally, chapter 7 summarizes the findings in this thesis.

Chapter 2

Theoretical Considerations

The interstellar magnetic field, ubiquitous in the Galaxy, although in small magnitude in diffuse medium (a most probable maximum value $\sim 10~\mu$G at low volume density is given by Crutcher et al. 2010), would interact with gas and dust and shape their dynamics. The VChG is a statistical technique trying to produce synthetic dust polarization maps by HI observation, whose highly simplified logic is to first measure the anisotropy of HI using gradient method and then predict the magnetic field/ dust polarization using such HI anisotropy. Therefore, in this chapter, I will investigate the theoretical considerations of the VChG method, by viewing how the gas, dust and interstellar magnetic field interact with each other, as well as why the gradient method works.

2.1 From HI to magnetic field

The observation that the morphology of HI correlates with the direction of interstellar magnetic fields is actually not a coincidence, but a phenomena with theoretical support. In this section, I will introduce the underlying theories from three aspects, the MHD description of HI, the flux freezing theorem and MHD turbulence.

2.1.1 MHD description of HI

The HI gas exists in two phases, warm HI and cool HI (McKee & Ostriker, 1977). The cool HI is denser with number density $n_H \sim 30$ cm^{-3}. It occupies $\sim$ 1% out of the total local interstellar volume, which exists in cloudy structures. The more tenuous warm HI ($n_H \sim 0.6$ cm^{-3}) occupies $\sim 40\%$ volume of local interstellar space, which exists in diffuse structures. It is necessary to point out that although the HI is defined as neutral hydrogen, such neutral medium is actually not perfectly neutral, but partially ionized by starlight photons and cosmic rays. More exactly, the warm HI ($T \sim 5000$ K) is ionized by a fraction ~ 0.02; the cool HI ($T \sim 100$ K) is ionized by a fraction $\sim 3 \times 10^{-4}$ (Draine, 2011). Hence, the dynamics of HI would be influenced by interstellar magnetic field.

For the continuous ionized or partially ionized medium, it would be convenient to describe by plasma, a quasi-neutral system consisting of plenty of charged particles with collective behavior. More strictly speaking, as the matter to to exist in plasma state, three criteria (Callen, 2006) have to be met

- The length scale of the studied system, L, is much larger than the Debye length λ_D

$$L >> \lambda_D \ , \tag{2.1}$$

  which, due to Debye shielding, makes sure the plasma bulk is dominated by collective interactions instead of local Coulomb interactions.

- The number of charged particles within the Debye sphere, $\Lambda = \frac{4\pi}{3} n_e \lambda_D^3$, is much larger than 1

$$\Lambda >> 1 \ , \tag{2.2}$$

  which is the most essential requirement among three criteria (Chen, 2016), a necessity that there are enough charged particles for Debye shielding.

- The plasma oscillation frequency (or Langmuir frequency; Tonks & Lang-

muir 1929), f_{pe}, representing the electrical interactions, is much larger than the electron-neutral collision frequency, ν_{en}, representing the non-electrical interactions

$$f_{pe} >> \nu_{en} \ , \tag{2.3}$$

so that the electrical interactions within plasma are not dissipated by the collisions with neutral particles.

According to definition, the Debye length considering the electrons is (the contribution from ions can be neglected)

$$\lambda_D = \sqrt{\frac{\epsilon_0 k_B T}{n_e e^2}} \approx 690 (\frac{T}{10^4 K})^{\frac{1}{2}} (\frac{cm^{-3}}{n_e})^{\frac{1}{2}} \text{ cm} \ . \tag{2.4}$$

The Langmuir frequency is

$$f_{pe} = \frac{1}{2\pi} \sqrt{\frac{n_e e^2}{m_e \epsilon_0}} \approx 9000 \sqrt{\frac{n_e}{cm^{-3}}} \text{ Hz} \ . \tag{2.5}$$

Since that the ionization fraction of HI is low and electrons move much faster than hydrogen atoms, we can approximately treat it as electrons collide with stationary hydrogen "forest". The electron-neutral collision frequency can be calculated by

$$\nu_{en} = n_H < \sigma v_e > \ , \tag{2.6}$$

where the cross section σ can be estimated by treating the particles as hard solid spheres and, considering the supersonic motion, the speed of electrons v_e can be estimated by electron's mean thermal speed. Thus, the electron-neutral collision frequency can be given (a more accurate formula is given later at Equation 2.16 while the results the same)

$$\nu_{en} \approx n_H (4\pi r_H^2)(\sqrt{\frac{8k_B T}{\pi m_e}}) \ , \tag{2.7}$$

where the r_H is the radius of hydrogen atom. From the equations above, we

Phase	n_H (cm^{-3})	n_e (cm^{-3})	T (K)	λ_D (cm)	Λ	f_{pe} (Hz)	ν_{en} (Hz)
Warm HI	0.6	0.012	5000	4000	10^9	1000	8×10^{-9}
Cool HI	30	0.009	100	700	10^7	800	6×10^{-8}

Table 2.1: Estimations of critical plasma parameters for two phases of HI. To be clear, results only keep one significant number or order of magnitude.

can find that those critical plasma parameters merely depend on temperature and number density. Substituting the conditions of warm and cool HI into equations, those critical parameters can be obtained as shown in Table 2.1. From the table, also considering that our spacial scale of study is $\gtrsim 1$ pc ($\gtrsim 3 \times 10^{16}$ m), the three plasma criteria are perfectly met for both warm HI and cool HI. Therefore, we are able to describe the HI by magnetohydrodynamics (MHD) equations.

2.1.2 Flux freezing theorem

As a continuous, non-relativistic plasma, dynamics of the HI can be fully described by MHD equations, a combination of Maxwell's equations, Ohm's law and fluid equations. We are interested in the properties of HI revealed by the MHD equations (more details can be found in Priest 2014 Chapter 2). To begin with, the differential form of Faraday's Law and Ampère's Law can be written

$$\nabla \times \mathbf{B} = \mu \mathbf{j} \tag{2.8}$$

$$\nabla \times \mathbf{E} = -\frac{\partial \mathbf{B}}{\partial t} \ , \tag{2.9}$$

where since the HI is non-relativistic ($v << c$), the displacement current term $\frac{1}{c^2}\frac{\partial \mathbf{E}}{\partial t}$ is negligible hence not shown in the Faraday's law. Meanwhile, the Ohm's Law can be written

$$\mathbf{j} = \sigma(\mathbf{E} + \mathbf{v} \times \mathbf{B}) \ , \tag{2.10}$$

where σ is the electrical conductivity. Combining the equations Equation 2.8 – 2.10 and eliminating $\mathbf{E}$ and $\mathbf{j}$ yields the induction equation

$$\frac{\partial \mathbf{B}}{\partial t} = \nabla \times (\mathbf{v} \times \mathbf{B}) + \eta \nabla^2 \mathbf{B} \ , \tag{2.11}$$

where η is the magnetic diffusivity $\eta = \frac{1}{\mu\sigma}$. The first term $\nabla \times (\mathbf{v} \times \mathbf{B})$ is the convective term and the second $\eta\nabla^2\mathbf{B}$ is the diffusive term. The ratio of the magnitude of two terms is the magnetic Reynolds number R_m

$$R_m = \frac{\frac{v_0 B_0}{l_0}}{\eta \frac{B_0}{l_0^2}} = \frac{v_0 l_0}{\eta} = v_0 l_0 \mu \sigma \ , \tag{2.12}$$

where the subscript "0" denotes the magnitude of variables that we study. When $Rm \gg 1$, the diffusive term becomes negligible compared with the convective term, which makes the ideal limit of MHD equations. Under such ideal limit, the total differential of the magnetic flux through surface $\mathbf{S}$ bounded by curve C

$$\begin{aligned}
\frac{d}{dt}\Phi &= \frac{d}{dt}\iint_S \mathbf{B} \cdot d\mathbf{S} \\
&= \iint_S \frac{\partial \mathbf{B}}{\partial t} \cdot d\mathbf{S} + \oint_C \mathbf{B} \cdot \mathbf{v} \times d\mathbf{l} \\
&= \iint_S \left(\frac{\partial \mathbf{B}}{\partial t} - \nabla \times (\mathbf{v} \times \mathbf{B}) \right) \cdot d\mathbf{S} \\
&= 0
\end{aligned} \tag{2.13}$$

equals zero, where the surface $\mathbf{S}$ moves with the plasma. Therefore, as a consequence of ideal induction equation, the magnetic flux is conserved. Or, in other words, the magnetic field is frozen into the plasma (Alfvén's flux freezing theorem; Alfvén 1942). Driven by Lorentz force, the morphology of plasma would align with the magnetic fields, which explains the alignment between HI structures and interstellar magnetic fields. While, one should keep in mind that the flux freezing theorem only applies to ideal plasmas, with $R_m \gg 1$.

To check the applicability of the theorem, we need to estimate the R_m of HI.

In warm HI, the main ion component is H$^+$, or proton, so we can simplify the plasma as a soup of neutral hydrogen atom H, electrons and protons. Due to the small ionization fraction, the diffusion arising from interaction between ions and neutrals now matters (known as ambipolar diffusion). Namely, when the ionization fraction is extremely small, the collisions between ions and neutrals would be relatively more important than the collisions between electrons and ions/ neutrals, which to large extent decreases the conductivity of plasma. To evaluate the diffusion by neutrals, a complete description of conductivity (Cowling conductivity; Priest 2014) is

$$\sigma_C = \left[\frac{m_e(\nu_{ei} + \nu_{en})}{n_e e^2} + \frac{(1-x)^2 B^2}{n_e m_e \nu_{in}}\right]^{-1} , \qquad (2.14)$$

where x is the ionization fraction; B is the magnetic field strength; ν_{ei} is the collision frequency between electrons and ions (protons in this case)

$$\nu_{ei} = 3.759 \times 10^{-6} n_e T^{-\frac{3}{2}} \ln \Lambda ; \qquad (2.15)$$

ν_{en} is the collision frequency between electrons and neutrals

$$\nu_{en} = 1.95 \times 10^{-16} n_n T^{\frac{1}{2}} ; \qquad (2.16)$$

ν_{in} is the collision frequency between protons and neutrals (Pontieu et al., 2001)

$$\nu_{in} = 1.03 \times 10^{-16} n_i T^{1/2} . \qquad (2.17)$$

In the last equations all quantities are in SI units. To estimate R_m for warm HI we now need to substitute σ_C from Equation 2.14 into Equation 2.12.

In cool HI, with even lower temperature, ionization of hydrogen becomes more difficult and meanwhile heavier elements (metals) contribute relatively more to providing charged ions and free electrons. Both protons and metal

ions would interact with the neutrals and make the collision frequency harder to calculate. Hence, in this place we directly cite the results from Krumholz (2015) that the magnitude of the magnetic Reynolds number arising from ambipolar diffusion is

$$R_m = \frac{4\pi l_0 v_0 \rho^2 x \gamma}{B^2} \ ,$$

(2.18)

where ρ is the density of hydrogen and γ is a "drag" coefficient from ions. By Smith & Mac Low (1997), the coefficient is estimated to be $\gamma \approx 9.2 \times 10^{13}$ cm^{3}s^{-1}.

In our application, the spacial length scale is $l_0 \gtrsim 1$ pc; the velocity scale for HI is $v_0 \sim 10$ km s^{-1} and the interstellar magnetic field is ~ 10 μG. Therefore, substituting all the numbers into Equation 2.12 and Equation 2.18, we are able to estimate the magnetic Reynolds numbers of warm and cool HI, which both are $R_m \sim 50$. In the scale ~ 1 pc, the minimal scale that the VChG method extract anisotropy in this thesis, the HI is ionized enough to be relatively ideal plasma (although not perfect), where the magnetic diffusion is small and the flux freezing theorem holds. This explains why the HI follows interstellar magnetic fields and why ideal MHD equations are applicable to HI.

2.1.3 MHD turbulence

When the Reynolds number is extremely high, $Re \gtrsim (3-5) \times 10^3$, the laminar flow of the fluid would become chaotic, whirlwind and turbulent. Kolmogorov (1941) depicted the picture of incompressible turbulence as a cascade-like eddies system, where at large scale the energy is injected and the large eddies are created, while due to their instability the large eddies break and transfer kinetic energy to smaller eddies, until when the energy is dissipated by viscosity at small scale with low Reynolds number. In the famous Kolmogorov's isotropic turbulence, at the scale smaller than injection scale L but larger than dissipation scale, the energy spectrum only depends on the rate of energy dissipation

$$E(k) \sim \epsilon^{2/3} k^{-5/3} \;, \tag{2.19}$$

where k is the wave number, corresponding to the spatial scale as $\lambda = 2\pi/k$. Note that the energy spectrum is a total power in the interval of wave number $k, k+dk$, thus is related to the power spectrum as $E(k)dk = \int d\Omega_{\mathbf{k}} P(\mathbf{k}) k^{D-1} dk$ for number of dimensions D. The power spectrum in a two-dimensional (2D) distribution field is $P \propto k^{-8/3}$ and that in three-dimensional (3D) is $P \propto k^{-11/3}$ (Elmegreen & Scalo, 2004). A power spectrum with index ~ -3.7 between scale 2×10^6 m $\sim 10^{13}$ m in the local ISM (< 1 kpc) was obtained by Armstrong et al. (1995). Particularly, the 2D power spectrum of HI emission in Galactic plane was observed by Green (1993) with a power index $-2.2 \sim -3.0$ and later the 3D power spectrum of HI emission at high Galactic latitude was observed by Miville-Deschênes et al. (2003) with a power index $\sim -3.6 \pm 0.2$. These results are comparable to the Kolmogorov power spectra indexes and thus supports that the local ISM including HI is turbulent in Kolmogorov's picture.

When the magnetic field becomes important for the fluid, with energy density of magnetic field comparable to the kinetic energy density of turbulence, the turbulence will be anisotropic, a quantitative description of which was given by Goldreich & Sridhar (1995). The relation between parallel and perpendicular scales initially formulated for the mean system reference frame by the authors can be written in the local reference frame as (Brandenburg & Lazarian, 2013)

$$l_{\parallel}^{-1} V_A \approx l_{\perp}^{-1} V_l \;, \tag{2.20}$$

where V_A is the Alfvén speed, V_l is the eddy velocity, and $l_{\parallel}$ and $l_{\perp}$ are the eddy scales parallel and perpendicular to the local direction of the magnetic field, respectively. The importance of the magnetic field in turbulent cascade is usually characterized by the Alfvénic Mach number which is the ratio of velocities at the injection scale L to Alfvén velocity, $M_A = V_L/V_A$.

The concept of the eddies tracing the local magnetic field was confirmed in numerical simulations (see Cho & Vishniac 2000; Maron & Goldreich 2001; Cho et al. 2002) and it has become an essential element of the modern theory of MHD turbulence.

This concept is also crucial for understanding how magnetic field tracing with velocity gradients works. From the relation in Equation 2.20 we can see that eddies are elongated along the magnetic field and the elongated eddies have the largest velocity gradient perpendicular to the longest axes of eddies. Thus, we expect the direction of the maximum velocity gradient to be perpendicular to the local magnetic field (aforementioned elongated direction). In this way, accounting for the 90 degrees angle difference, the velocity gradients can trace the directions of the local magnetic field.

As mentioned at section 1.3 and will be explained in more details at section 2.2, the long axes of dust grains are aligned perpendicular to local magnetic fields, which is used as the most accepted way of magnetic field tracing (Lazarian, 2007). The thermal dust polarization is along the long dust grain axes and, as a result, dust emission polarization and velocity gradients are both perpendicular to magnetic field. This opens a possibility to use velocity gradients to predict the polarization arising from the aligned dust and interfering with the CMB polarization studies. Indeed, atomic hydrogen and dust are well mixed at high galactic latitudes. Therefore the velocity gradients obtained with 21 cm emission can be used to predict the polarization from the dust. In this thesis, we explore the accuracy of this approach.

2.2 Interstellar magnetic field and dust polarization

Traditionally, there are two scenarios where one talks about the dust polarization, absorption and emission (see Andersson et al. 2015 for a review). The
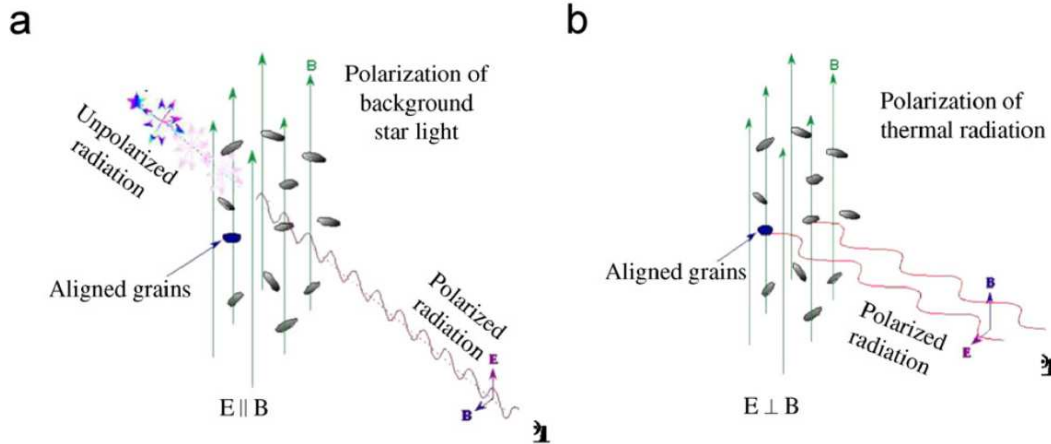
Figure 2.1: The sketch for starlight polarization (panel a) and thermal dust polarization (panel b). Credit: Lazarian (2007).

polarized radiation from distant stars was first observed by Hall (1949) and Hiltner (1949a). Such polarization was quickly attributed to the intervening interstellar dust grains, which aligned with the magnetic field (Hiltner, 1949b). We are interested in the thermal dust emission that is also linearly polarized (Stein, 1966) and was first observed by Cudlip et al. (1982) at far infrared wavelength. The direction of polarization of the radiation emitted by thermal dust is expected to be perpendicular to the magnetic field.

Actually, the basic origin of dust polarization can be explained by a combination of three conditions

1. The dust grains are aspherical.

2. The dust grains preferentially extinct (i.e. absorb and scatter) or emit E-component radiation along their long axes (Lazarian & Finkbeiner, 2003).

3. The dust grains tend to align perpendicular to the magnetic field.

The first two are natural, while the third one, how and in which condition the grains align with the magnetic field, remains a complex question for the community. So far, three theoretical grain alignment models remains the main

candidates, paramagnetic alignment (Davis & Greenstein 1951; Purcell 1979; Mathis 1986), mechanical alignment (Gold, 1952) and radiative torque (RAT; Dolginov & Mitrofanov 1976; Draine & Weingartner 1996; Lazarian & Hoang 2007a) alignment. Among them, considering a series of theoretical and observational tests, the RAT model looks the most promising (Andersson et al., 2015), thus also the one to be primarily introduced here. A brief logic for the RAT alignment mechanism is that, being exposed to an anisotropic radiation field, the aspherical grains will acquire angular momentum and spin up driven by the differential torques from the left-hand circular (LHC) and right-hand circular (RHC) components of the radiation. Meanwhile, as paramagnetic material, the grains will acquire magnetic moments due to Barnett effect (Barnett, 1935) and thus align perpendicular to magnetic field in Larmor precession. Note that the RAT alignment mechanism works efficiently only when the radiation wavelength is comparable or smaller than the dust grain sizes.

Therefore, the two instances of polarization are natural consequences of the dust alignment mechanism. Since long axis of grains align perpendicular to the magnetic field, dust extinction or emission would be more efficient perpendicular to magnetic field while less efficient along magnetic field. In the starlight dust absorption case, as shown in Figure 2.1a, given the background unpolarized radiation is preferentially absorbed perpendicular to the magnetic field, the observed radiation would be partially polarized along the magnetic field,

$$P_{\mathrm{abs}} = \frac{\mathrm{e}^{-\tau_\parallel} - \mathrm{e}^{-\tau_\perp}}{\mathrm{e}^{-\tau_\parallel} + \mathrm{e}^{-\tau_\perp}} \approx - \left(\tau_\parallel - \tau_\perp \right) / 2 \; , \qquad (2.21)$$

with the approximation $\tau_\parallel - \tau_\perp \ll 1$, where the $\tau_\parallel$ and $\tau_\perp$ are the optical depths due to dust absorption for radiation with parallel and perpendicular polarizations to the magnetic field, respectively. Starlight extinction due to dust is observed in optical and infrared spectral bands.

The thermal dust emission takes place at microwave to sub-millimeter wave-

lengths. As shown in Figure 2.1, dust grains radiate preferentially perpendicular to the magnetic field, thus the observed radiation would be partially polarized perpendicular to the magnetic field,

$$P_{\text{em}} = \frac{(1 - \mathrm{e}^{-\tau_\parallel}) - (1 - \mathrm{e}^{-\tau_\perp})}{(1 - \mathrm{e}^{-\tau_\parallel}) + (1 - \mathrm{e}^{-\tau_\perp})} \approx \frac{\tau_\parallel - \tau_\perp}{\tau_\parallel + \tau_\perp} \ . \tag{2.22}$$

Note that the optically-thin approximation is taken for both cases, namely, $\tau_\parallel << 1, \tau_\perp << 1$. Furthermore, the relationship between dust polarization and magnetic field permits the method to observe magnetic field by polarimetry (Lazarian, 2003). In this thesis, looking at the foreground contamination at frequencies $\gtrsim 100$ GHz, we focus on the thermal dust emission, which connects with the interstellar magnetic fields by a 90° rotation.

It worth mentioning that, besides the thermal dust contribution, the swiftly spinning dust grains, with dipole moments, would produce microwave emission at $\sim 10 - 100$ GHz (Erickson 1957; Draine & Weingartner 1996; Draine & Lazarian 1998; Hoang & Lazarian 2012). Some anomalous excess of microwave emission (AME) in intensity maps at these frequencies has been observed in Planck Collaboration et al. (2011b) and Planck Collaboration et al. (2014), though interpretation of it as coming from a spinning dust is uncertain. However, the radiation from spinning dust is expected to be only few percent polarized (Lazarian & Draine, 2000) due to smallness of the spinning dust particles, which is small compared with synchrotron or thermal dust polarization. As well the spinning dust polarization peaks at low frequencies, so it was ignored in Planck foreground polarization separation (Planck Collaboration et al., 2016c) for channels covered by HFI instrument that start at 100 GHz. Thus, in this thesis, we do not consider spinning dust either but focus on the main source of foreground dust polarization, the thermal dust polarization.

2.3 Mathematical foundation for gradient method

Let us briefly discuss the mathematical foundations of the gradient methods in application to study of the direction of the magnetic field. Observing emission from the turbulent media, one constructs the sky maps of different observables that describe the emission. First of all, this is the intensity of the emission in PPV (position-position $\mathbf{X}$-velocity v) space $I(\mathbf{X}, v)$, and the related integrated quantities, such as the total intensity and (un-normalized) velocity centroids which for optically thin lines are $I_c(\mathbf{X}) \propto \int dv I(\mathbf{X}, v)$ and $VC(\mathbf{X}) \propto \int v dv I(\mathbf{X}, v)$ respectively. The maps represent random fluctuating fields.

The simplest local statistical measure of the gradient of a random field $f(\mathbf{x})$ is the gradient covariance tensor

$$\sigma_{\nabla_i \nabla_j} \equiv \langle \nabla_i f(\mathbf{X}) \nabla_j f(\mathbf{X}) \rangle = \nabla_i \nabla_j D(\mathbf{R})|_{\mathbf{R} \to 0} , \qquad (2.23)$$

which is the zero separation limit of the second derivatives of the field structure function $D(\mathbf{R}) \equiv \frac{1}{2} \langle (f(\mathbf{X} + \mathbf{R}) - f(\mathbf{X}))^2 \rangle$ (to simplify further notation we define the structure function with a non-standard coefficient $1/2$).

For a statistically isotropic field, the covariance of the gradients is isotropic, $\sigma_{\nabla_i \nabla_j} = \frac{1}{2} \delta_{ij} \Delta D(R)|_{R \to 0}$. However, as was studied in Lazarian & Pogosyan (2012) for synchrotron, Kandel et al. (2016) for velocity channel intensities and Kandel et al. (2017) for velocity centroids, in the presence of the magnetic field, the structure function of the signal becomes orientation dependent, depending on the angle between $\mathbf{R}$ and the projected direction of the magnetic field. This anisotropy is retained in the limit $\mathbf{R} \to 0$ and results in non-vanishing traceless

part of the gradient covariance tensor

$$\sigma_{\nabla_i \nabla_j} - \frac{1}{2}\delta_{ij} \sum_{l=1,2} \sigma_{\nabla_l \nabla_l} =$$

$$\frac{1}{2}\begin{pmatrix} \left(\nabla_x^2 - \nabla_y^2\right)D(\mathbf{R}) & 2\nabla_x\nabla_y D(\mathbf{R}) \\ 2\nabla_x\nabla_y D(\mathbf{R}) & \left(\nabla_y^2 - \nabla_x^2\right)D(\mathbf{R}) \end{pmatrix}_{\mathbf{R}\to 0} \neq 0 \ . \qquad (2.24)$$

The eigendirection of the covariance tensor that corresponds to the largest eigenvalue ("the direction of the gradient") then makes an angle θ with the coordinate x-axis

$$\tan\theta = \frac{2\nabla_x\nabla_y D}{\sqrt{\left(\nabla_x^2 D - \nabla_y^2 D\right)^2 + 4\left(\nabla_x\nabla_y D\right)^2} + \left(\nabla_x^2 - \nabla_y^2\right)D} \ . \qquad (2.25)$$

Anisotropic structure functions can be decomposed in angular harmonics. In Fourier space, where

$$D(\mathbf{R}) = \int d\mathbf{K}\, P(\mathbf{K})\left[1 - e^{i\mathbf{K}\cdot\mathbf{R}}\right] \ , \qquad (2.26)$$

this decomposition is over the dependence of the power spectrum $P(\mathbf{K})$ on the angle of the 2D wave vector $\mathbf{K}$. Denoting the coordinate angle of $\mathbf{K}$ by θ_K and that of the projected magnetic field as θ_H, we have for the spectrum

$$P(\mathbf{K}) = \sum_n P_n(K)e^{in(\theta_H - \theta_K)} \qquad (2.27)$$

and for the derivatives of the structure function

$$\nabla_i\nabla_j D(\mathbf{R}) =$$

$$= \sum_n \int K^3 P_n(K) \int d\theta_K e^{in(\theta_H - \theta_K)} e^{iKR\cos(\theta_R - \theta_K)} \widehat{K}_i\widehat{K}_j \ , \qquad (2.28)$$

where hat designates unit vectors, namely $\widehat{K}_x = \cos\theta_K$ and $\widehat{K}_y = \sin\theta_K$, and

θ_R is the coordinate angle of the radius vector $\mathbf{R}$. Performing integration over θ_K, we obtain the traceless anisotropic part

$$(\nabla_x^2 - \nabla_y^2)D(\mathbf{R}) = \pi \sum_n i^n e^{in(\theta_H - \theta_R)} \times \tag{2.29}$$

$$\times \int dK K^3 J_n(kR) \left(P_{n-2}(K)e^{-i2\theta_H} + P_{n+2}(K)e^{i2\theta_H} \right)$$

$$\nabla_x \nabla_y D(\mathbf{R}) = \frac{\pi}{2i} \sum_n i^n e^{in(\theta_H - \theta_R)} \times \tag{2.30}$$

$$\times \int dK K^3 J_n(kR) \left(-P_{n-2}(K)e^{-i2\theta_H} + P_{n+2}(K)e^{i2\theta_H} \right) \ .$$

In the limit $R \to 0$, only the $n = 0$ term for which $J_0(0) = 1$ survives, θ_R dependence drops out, and we have

$$(\nabla_x^2 - \nabla_y^2)D(\mathbf{R}) = \left[2\pi \int dK K^3 P_2(K) \right] \cos 2\theta_H \tag{2.31}$$

$$2\nabla_x \nabla_y D(\mathbf{R}) = \left[2\pi \int dK K^3 P_2(K) \right] \sin 2\theta_H \ . \tag{2.32}$$

Notice that anisotropy of the gradient variance is determined by the quadrupole of the power spectrum (and structure function). Substituting this result into Equation 2.25, we find that the eigendirection of the gradient variance has the form

$$\tan \theta = \frac{A \sin 2\theta_H}{|A| + A \cos 2\theta_H} = \begin{cases} \tan \theta_H & A > 0 \\ -\cot \theta_H & A < 0 \end{cases} \tag{2.33}$$

and is either parallel or perpendicular to the direction of the magnetic field, depending on the sign of $A \propto \int dK K^3 P_2(K)$, i.e the sign of the spectral quadrupole P_2.

Since the direction of the magnetic field that we aim to track is unsigned, it is appropriate to describe it as an eigendirection of the rank-2 tensor, rather than a vector. This naturally leads to the mathematical formalism of Stokes parameters. As the local estimator of the angle θ via the gradients, we can

introduce pseudo-Stokes parameters

$$\widetilde{Q} \propto (\nabla_x f)^2 - (\nabla_y f)^2 \propto \cos 2\theta \tag{2.34}$$

$$\widetilde{U} \propto 2\nabla_x f \nabla_y f \propto \sin 2\theta \tag{2.35}$$

so that

$$\frac{\widetilde{U}}{\widetilde{Q}} = \tan 2\theta \sim \tan 2\theta_H \ . \tag{2.36}$$

In the next section, we describe the exact procedure for the estimator that we use in this paper.

The pseudo Stokes parameters naturally connect the gradient techniques with polarization studies. More exactly, both for synchrotron (Lazarian & Pogosyan 2012; Kandel et al. 2018) and thermal dust emission (Clark et al. 2015; Caldwell et al. 2017; Kandel et al. 2018, see Crutcher et al. 2010 and references therein), we expect the true polarization Stokes parameters to be

$$Q \propto \int dz (H_x^2 - H_y^2) \propto \cos 2\theta_H \tag{2.37}$$

$$U \propto \int dz 2H_x H_y \propto \sin 2\theta_H \ . \tag{2.38}$$

Thus, the pseudo Stokes parameters constructed from the gradients can be directly compared with Stokes parameters that probe polarized emission in magnetized medium.

Chapter 3

Method

3.1 Main steps

Making use of the optically thin emission line maps in PPV space, such as HI 21cm maps, we are able to determine the direction of the magnetic field through our new method. In this method, we focus on obtaining the maximum information from the motions of the gas by using full resolution velocity channel slices of PPV cube. It consists of the following steps:

1. As a first preparatory step, to have robust control of intensity gradient determination at the pixel level, full spatial resolution individual velocity channel maps I($\mathbf{X}$,v) are smoothed by a Gaussian filter with $FWHM = 3$ pixels. The direction of the gradient at each pixel $p = (i, j)$ is defined as

$$\theta_p(i, j) = \text{atan}\left[\frac{I(i, j + 1) - I(i, j - 1)}{I(i + 1, j) - I(i - 1, j)}\right] \quad , \tag{3.1}$$

which is on the rectangular grid with nodes at coordinates $\mathbf{X}(i, j)$. Here (i, j) are the indexes of raw pixels. The magnitude of the gradient is not used.

2. The map is then segmented into coarse-grained super-pixel blocks, over which the average direction of the gradient is defined by calculating the

35

mean $\overline{\cos 2\theta_p}$ and $\overline{\sin 2\theta_p}$ within each block $B = (I, J)$. Here (I, J) are the indexes of super-pixels blocks. We have chosen these coarse-grained super-pixels to be square blocks of 60×60 pixels as a compromise between the final resolution of the reconstruction and necessity to have sufficient statistics within a block. The technical details of how the averaging is performed are given in section 3.2.

Finding as well the total intensity in the block, we define a set of coarse-grained pseudo Stokes parameters for each velocity channel:

$$I_B(I, J, v) = \sum_{p \in B} I_p(v) \ , \tag{3.2}$$

$$\widetilde{Q}_B(I, J, v) = I_B \overline{\cos 2\theta_p} \ , \tag{3.3}$$

$$\widetilde{U}_B(I, J, v) = I_B \overline{\sin 2\theta_p} \ , \tag{3.4}$$

where tilde signifies the pseudo nature of these "polarization" parameters (since HI emission is not polarized). The (intensity independent) direction and degree of "polarization" in each super-pixel are[1]:

$$\theta_B(I, J, v) = \frac{1}{2} \mathrm{atan2} \left(\overline{\sin 2\theta_p}, \ \overline{\cos 2\theta_p} \right) \tag{3.5}$$

$$p_B(I, J, v) = \sqrt{(\overline{\cos 2\theta_p})^2 + (\overline{\sin 2\theta_p})^2} \leq 1 \tag{3.6}$$

Here we note that averaged $\overline{\cos 2\theta_p}$ and $\overline{\sin 2\theta_p}$ squared do not, in general, add to unity, so the procedure describes depolarization due to variation of directions within the super-pixel block.

3. At the last step of our VChG method, using additivity property of Stokes parameters when emission is combined, we sum over all velocity channels

---

[1]Here and below we are using atan2(y, x) function for quadrant-aware inverse tangent of y/x

to obtain the total coarse grained maps of pseudo Stokes parameters:

$$I_{VChG}(I, J) = \sum_v I_B(I, J, v) \tag{3.7}$$

$$\tilde{Q}_{VChG}(I, J) = \sum_v \widetilde{Q}_B(I, J, v) \tag{3.8}$$

$$\tilde{U}_{VChG}(I, J) = \sum_v \widetilde{U}_B(I, J, v) \tag{3.9}$$

and of the final direction angle and "polarization" degree:

$$\theta_{VChG}(I, J) = \frac{1}{2}\mathrm{atan2}\left(\widetilde{U}_{VChG}(I, J), \widetilde{Q}_{VChG}(I, J)\right) \tag{3.10}$$

$$p_{VChG}(I, J) = \sqrt{\widetilde{Q}_{VChG}(I, J)^2 + \widetilde{U}_{VChG}(I, J)^2}/I_{VChG}(I, J) \ . \tag{3.11}$$

Using Stokes parameters to propagate information about direction of the gradients, as well as the level of their variance within the coarse grained pixel, allows us to use the final $I, \tilde{Q}, \tilde{U}$ maps in two-fold way. As far as the direction only is concerned, they give the prediction for the direction of the magnetic field. But if we also use the observational fact that HI intensity distribution closely follows that of the thermal dust, we can consider our pseudo-Stokes maps as a prediction from HI data for the polarized dust emission.

3.2 Evaluation of the mean direction on coarse grained map

The fundamental step of our method is to define the averaged direction of PPV maps' gradients within a coarse grained block. We investigate two methods, both based on fitting the measured histogram of angle distribution within coarse grained block with analytical formulas. The difference is the choice of the fitting model.

The first approach has a simple theoretical foundation. As a model distribu-

tion of the gradient angular direction $\theta_p = \text{atan}\left[\nabla_y I(i,j,v)/\nabla_x I(i,j,v)\right]$, $p \in B$, we take the distribution that follows from assuming the gradients to be Gaussian with the covariance matrix $\widetilde{\sigma}_{ij}$ of Equation 2.23. The expression for this distribution can be easily found to be

$$P(\theta_p) = \frac{1}{\pi\sqrt{|\widetilde{\sigma}_{ij}|}}\left[\begin{pmatrix}\cos\theta_p \\ \sin\theta_p\end{pmatrix}\widetilde{\sigma}_{ij}^{-1}\begin{pmatrix}\cos\theta_p \\ \sin\theta_p\end{pmatrix}\right]^{-1} \tag{3.12}$$

$$= \frac{1}{\pi} \times \frac{\sqrt{1-\widetilde{\mathcal{J}_2}}}{1 - \sqrt{\widetilde{\mathcal{J}_2}}\cos 2\left(\widetilde{\theta}_B - \theta_p\right)} \ . \tag{3.13}$$

This distribution function has two parameters: $\widetilde{\mathcal{J}_2}$ and $\widetilde{\theta}_B$. The first is the rotation invariant ratio of the determinant of the traceless part of the covariance matrix and the (half of) trace of the covariance

$$\widetilde{\mathcal{J}_2} \equiv \frac{(\widetilde{\sigma}_{xx} - \widetilde{\sigma}_{yy})^2 + 4\widetilde{\sigma}_{xy}^2}{(\widetilde{\sigma}_{xx} + \widetilde{\sigma}_{yy})^2} \tag{3.14}$$

and the second is the angle

$$\tan 2\widetilde{\theta}_B \equiv \frac{2\widetilde{\sigma}_{xy}}{\widetilde{\sigma}_{xx} - \widetilde{\sigma}_{yy}} \ . \tag{3.15}$$

They can be thought of as estimators (thus tilde) for the coarse grained combinations of covariance components of the gradient. The distribution in Equation 3.12 is periodic with a period π and is normalized to unity on any angular interval of the length of the period, $\int_{\theta_p^*}^{\theta_p^*+\pi} P(\theta_p)d\theta_p = 1$. The statistically isotropic case corresponds to $\widetilde{\sigma}_{xx} = \widetilde{\sigma}_{yy}$ and $\widetilde{\sigma}_{xy} = 0$, i.e $\widetilde{\mathcal{J}_2} = 0$ when Equation 3.12 evaluates to uniform distribution. Any anisotropy leads to non-zero $\widetilde{\mathcal{J}_2} > 0$, which on the other hand is bounded by definition not to exceed unity, $\widetilde{\mathcal{J}_2} \leq 1$. Note that fitting angular distribution does not determine the trace of gradient covariance $\widetilde{\mathcal{I}_1} = \widetilde{\sigma}_{xx} + \widetilde{\sigma}_{yy}$.

The average $\overline{\cos 2\theta_p}$ and $\overline{\sin 2\theta_p}$ are now readily obtained

$$
\begin{pmatrix} \overline{\cos 2\theta_p} \\ \overline{\sin 2\theta_p} \end{pmatrix} = \begin{pmatrix} \cos 2\widetilde{\theta_B} \\ \sin 2\widetilde{\theta_B} \end{pmatrix} \times \frac{1 - \sqrt{1 - \widetilde{\mathcal{J}}_2}}{\sqrt{\widetilde{\mathcal{J}}_2}} \; . \tag{3.16}
$$

From here, the coarse grained direction is simply given by the angle fit parameter

$$
\theta_B = \widetilde{\theta_B} \equiv \frac{1}{2}\mathrm{atan2}\left(2\widetilde{\sigma}_{xy}, \, \widetilde{\sigma}_{xx} - \widetilde{\sigma}_{yy}\right) \; , \tag{3.17}
$$

i.e the detected θ_B is given by the peak position of the fitted distribution. The degree of polarization is, as expected, a rotation invariant quantity:

$$
p_B = \frac{1 - \sqrt{1 - \widetilde{\mathcal{J}}_2}}{\sqrt{\widetilde{\mathcal{J}}_2}} \; . \tag{3.18}
$$

It varies from zero for isotropic case $\widetilde{\mathcal{J}}_2 = 0$ to unity for maximum anisotropy at $\widetilde{\mathcal{J}}_2 = 1$.

This formalism allows us to analyze the effect of noise on our estimators of the direction and the degree of polarization. Assuming that noise in gradient measurements is isotropic and uniform within the block B, with variance σ_N^2 in each gradient component, its effect is the addition to the diagonal in the gradient one-point covariance

$$
\begin{pmatrix} \widetilde{\sigma}_{xx} & \widetilde{\sigma}_{xy} \\ \widetilde{\sigma}_{xy} & \widetilde{\sigma}_{yy} \end{pmatrix} \rightarrow \begin{pmatrix} \widetilde{\sigma}_{xx} + \sigma_N^2 & \widetilde{\sigma}_{xy} \\ \widetilde{\sigma}_{xy} & \widetilde{\sigma}_{yy} + \sigma_N^2 \end{pmatrix} \tag{3.19}
$$

which affects only the trace $\mathcal{I}_1$, but not $\widetilde{\sigma}_{xx} - \widetilde{\sigma}_{yy}$ nor $\widetilde{\sigma}_{xy}$. Thus, we reach an important conclusion that our angle estimator is unbiased by, at least such an idealized, noise. The noise, of course, affects the error on the estimator by decreasing $\widetilde{\mathcal{J}}_2$ and, thus, increasing the variance of θ_p. Similarly, degree of polarization, p_B, is affected by noise via $\widetilde{\mathcal{J}}_2$ as well, which decreases p_B

with noise addition. Thus, our estimator underestimates true p_B if the data is assumed noiseless. This can be corrected for, if the noise level σ_N^2 is known, but to apply this correction one needs to determine the trace of the gradient covariance $\widetilde{\mathcal{I}}_1$ by a separate analysis. Moreover, if the full noise covariance is directly measured for the data, it can be corrected for in a general non-isotropic noise case.

In the second approach, we use a phenomenological fitting function inspired by Yuen & Lazarian (2017) that consists of the Gaussian and the flat component in the range of angles $[-\pi/2, \pi/2]$

$$P(\theta_p) = A \exp[-(\theta_p - \tilde{\theta}_B)^2/(2\sigma^2)] + C . \qquad (3.20)$$

The model contains three independent parameters, i.e. $\bar{\theta}, \sigma$ and A, with the fourth one, C, fixed by the normalization. Evaluating the averages $\overline{\cos 2\theta}$ and $\overline{\sin 2\theta}$, shows that $\theta_B = \tilde{\theta}_B$. The expression for p_B is also readily obtainable, but is rather cumbersome to present it here. In Figure 3.1, we demonstrate our analysis of the performance of both techniques based on four selected $1° \times 1°$ superpixels from GALFA-HI map. The chosen size of superpixels corresponds to 60×60 blocks of GALFA-HI $1'$ pixels. The pixels with relatively high degree of polarization (upper panels) exhibit well pronounced preferred direction with low uniform baseline component. The pixels of low polarization degree (lower panels) show almost uniform angle distribution within, with some fluctuations over it. We can conclude that degree of polarization also serves a role of the measure of how accurately the direction in the coarse grained block is determined. For an estimate of an error $\Delta\theta_B$ on the determined coarse grained direction θ_B, we note that the data is smoothed by the Arecibo telescope beam ($FWHM \sim 3.5'$) and our additional smoothing with Gaussian $FWHM = 3'$ window, to the combined smoothing of $FWHM \approx 4.6'$. Thus we effectively have $(60/4.6)^2 \approx 170$ independent data points in our superpixel, which results
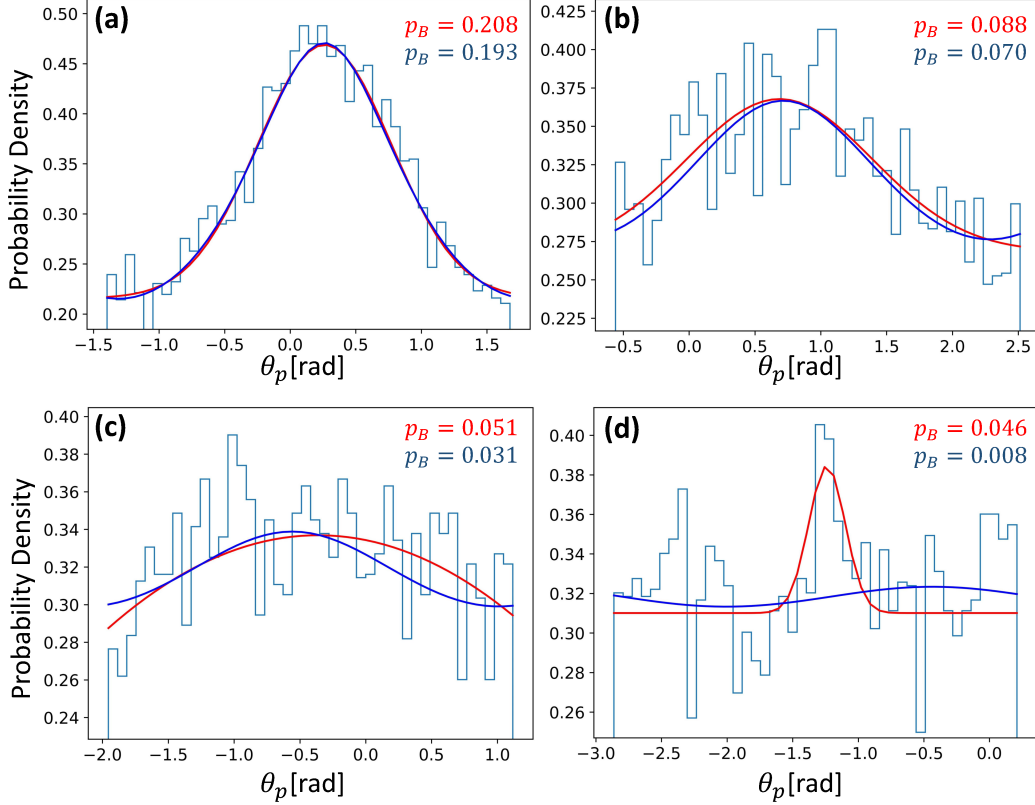
Figure 3.1: Examples of distribution of gradient directions θ_p within coarse grained pixels. Raw histograms and two model fits are shown. Blue curve - analytical Gaussian distribution for gradients, Equation 3.12. Red curve - phenomenological fit of Gaussian shape plus constant offset, Equation 3.20. The method's measurements of degree of polarization are given in each panel. Patch coherence and p_B decreases from panel (a) to panel (d). In the top row, both models give consistent determination of the coarse-grained direction, $\theta_B = 15°$ for both models in panel (a), and $\theta_B = 39°$ (red) and $\theta_B = 41°$ (blue) in panel (b). Panel (c) shows the case of wide distribution where non-periodic nature of the Gaussian curve leads to deviation, $\theta_B = -21°$ for the red model versus $\theta_B = -32°$ for the blue one. Panel (d) shows a highly noisy pixel where the red model picks a local peak at $\theta_B = -71°$, while the blue model shows almost flat distribution with $\theta_B = -25°$.

in an error estimate on the mean angle $\Delta\theta_B \approx \sigma_{\theta_p}/\sqrt{170} \approx \sigma_{\theta_p}/13$, where σ_{θ_p} is the variance of gradient angle θ_p within the superpixel[2].

The first method described fits the measured distributions extremely well in all cases, for high and low polarization degree. This, in particular, supports the idea that the gradients are nearly Gaussian distributed. The second, phenomenological choice of the fitting function performs very well and close to the first one for relatively high degree of polarization pixels. However, for low polarization pixels, where the direction is determined with high degree of uncertainty to start with, there are differences. Note that the constant term in Equation 3.20, while affecting the fit, does not contribute to the averages $\overline{\cos 2\theta}$ and $\overline{\sin 2\theta}$, and thus the resulting direction or polarization degree. These two quantities only come from the Gaussian term. With only one such term available for fit, the phenomenological formula effectively picks the most represented θ_p, eliminating the contribution of any other fluctuations in the angle histogram, akin of trying to find the direction which has the largest signal to noise. The first approach, on the other hand, fits faithfully variations in angle distribution and gives different result for near uniform distributions. As our comparison with observational data further in the text shows, phenomenological fits seem to perform marginally better in low polarization areas in determining the local direction θ_B. There is almost no difference between two methods for the polarization degree p_B. In what follows we show the numerical results from the phenomenological fit.

3.3   Relation to earlier studies

The idea of Velocity Channel Gradients (VChGs) as a means of tracing magnetic field was proposed in Lazarian & Yuen (2018a). This technique has been

---

[2]The error will be larger if *fluctuations* of the angle $\theta_p - \theta_B$ are significantly correlated at scales larger than $4.6'$.

successfully applied to studies magnetic field in diffuse atomic hydrogen as well as in molecular clouds (see González-Casanova & Lazarian 2019, Hu et al. 2019a). As an independent development, Clark et al. (2015, 2018) addressed a different problem of predicting polarized radiation from aligned dust using the technique of tracing HI intensity filaments within velocity channels. Reconstructed polarization maps can then be related to the magnetic field orientation.

Our modified VChG method shares some common features with these previous techniques, meanwhile making some improvements. In this section, we point out what we take from the previous work and what is different in our approach.

In the most general, and somewhat schematic sense, all methods of reconstruction of the magnetic field direction $\theta(\mathbf{X})$ from the velocity channel intensity $I(\mathbf{X}, v)$ have the structure:

$$\theta(\mathbf{X}) \sim \int dv \int d\mathbf{X}' \widehat{\mathcal{L}}_\theta\left(\mathbf{X}, \mathbf{X}', v\right) \int_{\delta v} dv' W\left(v, v'\right) I\left(\mathbf{X}', v'\right) \ , \qquad (3.21)$$

which consists of, right to left, a) assembly of the intensities in the synthetic velocity channel of the width δV and with weight W[3], b) action of an operator $\hat{L}$ on resulting intensity map, where $\hat{L}$ may be linear or non-linear, local or non-local, but is always anisotropic, carrying information on how the intensities reflect the direction of the magnetic field, and c) the final assembly over all the channels to obtain the sky map of angles (and/or polarization).

Among the steps above, the step b) is the central one, since that is where directional information is extracted. This paper develops the original idea of gradient technique of González-Casanova & Lazarian (2017), where $\widehat{\mathcal{L}}$ operator is factorized into evaluating the angle of the local gradient of the intensity map and subsequent averaging over some coarse grained resolution. Thus, the

---

[3]The width may be the whole line; the weight may include velocity itself, e.g., $W \sim v\delta(v - v')$, which gives velocity centroids, etc.

directional information is local, while further smoothing is direction-agnostic. An alternative notable technique of Clark et al. (2015) is based on Rolling Hough Transform (RHT), which in the disk of a given radius around every point on the map evaluates the radial integrated intensity as the function of direction, after the map was treated by high-pass filter, and some thresholding is applied. This procedure for determining direction is fundamentally non-local. Both approaches are non-linear in intensity, due to angle evaluation from the gradients, or intensity thresholding in RHT approach.

In the VChG of Lazarian & Yuen (2018a), the raw high resolution channel intensity maps, $I(\mathbf{X}, v)$, after first being smoothed with a Gaussian filter, are coadded over channels within the range δv_R around the average line center velocity v_0

$$I_p(\mathbf{X}) = \sum_{v_0 - \delta v_R/2}^{v_0 + \delta v_R/2} I_p(\mathbf{X}, v) \ . \tag{3.22}$$

The δv_R is chosen to be the *rms* velocity at spatial scale R, which makes the channel map under "thin channel regime" as defined in Lazarian & Pogosyan (2000). Then, gradients are calculated similarly to Equation 3.1 and Gaussian fitting to their distributions within coarse grained blocks is applied to determine the coarse grained map of angles $\theta_{VChG}(I, J)$.

We introduce the following changes relative to the original formulation

1. Instead of using integrated channel map, our new method calculate gradients using every channel map at raw spectroscopic resolution. According to Lazarian & Pogosyan (2000), thinner the channel is, more is it affected by the velocity fluctuations, which contribution, in turn, is more sensitive to anisotropic nature of MHD. As was numerically checked by Lazarian & Yuen (2018a), thinner channel results in higher tracing alignment measure of magnetic fields. Therefore, we calculate gradients in thinner channels then propagate through pseudo Stokes parameters. With much thinner channel maps used for calculation, it is natural to expect a better tracing

of magnetic fields.

2. Two methods are using different way to estimate gradients direction inside sub-blocks. The original VChG method fit the angle distribution by a Gaussian function of Equation 3.20 and choose the most probable angle to represent the coarse pixel. Whereas our new method focuses on evaluating mean values of $cos(2\theta_p)$ and $sin(2\theta_p)$ to define pseudo Stokes parameters for the coarse pixel. For high precision, this requires the phenomenological Gaussian fit (which is not periodic) to be performed iteratively adjusting the periodic interval of angles to obtain the mode of the distribution at the center. Our theory-inspired method is based on distribution of Equation 3.12, which automatically respects the periodicity condition. Our approach is more robust than that of the mode of the distribution, which, in particular, allowed us use narrow velocity channels. But more importantly, using information on the width of the angle distribution as well, we are able to depict a complete picture of the extent of angular variations inside the coarse pixel, which allows us to robustly estimate its degree of polarization.

The idea of extracting anisotropy at each velocity channel and propagating it by pseudo Stokes parameters was introduced to the field by Clark et al. (2015) and improved by Clark (2018). We similarly found this approach to be natural and useful, especially if the target is to compare with dust polarization maps, and we utilize it as well. The main difference between our method and Clark (2018) method is that we evaluate the anisotropy in individual channel by simply calculating linear gradients and then averaging in a coarse grained square pixel; Clark (2018) evaluates the anisotropy by angle averaging in RHT weighted pixels. Both methods produce pseudo Stokes parameter maps in velocity channels, $\tilde{Q}_B(v), \tilde{U}_B(v)$ and $Q_{RHT}(v), U_{RHT}(v)$, respectively. Once these quantities are defined, there is an additional significant difference between our

approaches. We treat $\tilde{Q}_B(v)$ and $\tilde{U}_B(v)$ as truly additive Stokes parameters which are directly co-added when velocity channels are combined. This carries forward information about variable degree of polarization in pixels across the sky in every channel. In Clark (2018) $Q_{RHT}(v)$ and $U_{RHT}(v)$ are used only to obtain the directional angle, which together with HI intensity $I_\nu(v)$ redefines the Stokes parameters to have uniform degree of polarization along the sky in individual channels. Note, that if the goal is to obtain the reconstruction of the magnetic field orientation, both approaches are only two of many possible ways to weight the orientation information in individual channels, where it remains to be studied which is the most optimal one. However, with regard to the degree of polarization, our method introduces the way to take pixel to pixel fluctuations of this quantity into the account which is missing in (Clark, 2018) approach.

The simplicity of our operator allows for a more straightforward theoretical analysis of its properties, as started in this paper. In particular, a notable difference comes from the local nature of our angle estimator versus RHT. With the knowledge of the gradient angular distribution within super-blocks, we are able to reveal more physical information, for example, Alfvénic Mach number (Lazarian et al. 2018; Hu et al. 2019a). Locality also gives us a straightforward way to include in the modelling the variations of the degree of polarization along the individual lines of sight that combine in the coarse grained pixel. These variations might reflect three dimensional fluctuations in the magnetic field along the line of sight, which is important for a more accurate modelling.

Chapter 4

Numerical test in different magnetization

As a new method to trace magnetic fields, we are interested in two things: the comparison with the original version of the VChG in terms of polarization orientation tracing and the VChG performance in media with different magnetization, namely, different Alfvénic Mach number. To do this, we test our method in simulation sets.

The simulation sets in this section are the same as in Lazarian & Yuen (2018a) and Lazarian et al. (2018), which adapted a series of compressible, turbulent, isothermal single fluid magnetohydrodynamic (MHD) simulations from ZEUS-MP/3D, a variant of the well-known code ZEUS-MP (Norman 2000, Hayes et al. 2006). Such simulations are characterized by two parameters, the Alfvénic Mach number $M_A = V_L/V_A$ that describes the role of the magnetic field, and the sonic Mach number $M_S = V_L/V_s$ given by the ratio of turbulent velocity at the injection scale to the sound speed, which describes the level of compressibility of the medium. Lower M_A means stronger effect of the magnetic field, and lower M_s means less compressible fluid. The subsonic cubes ($M_s \sim$ 0.9, M_A ranges from 0.09 to 0.94, see Table 4.1) with relatively low resolution, 480^3, allow us to take quick tests of our recipe. Meanwhile, the supersonic

Model	M_s	M_A	Resolution
Ms0.8Ma0.08	0.92	0.09	480^3
Ms0.8Ma0.264	0.98	0.32	480^3
Ms0.8Ma0.8	0.93	0.94	480^3

Table 4.1: Parameters of subsonic MHD simulation sets used. The Mach numbers in column "Model" are the initial values for a simulation. M_s and M_A are the instantaneous values at final snapshots. Resolution of the simulated cubes is 480^3.

Model	M_S	M_A	Resolution
Ma0.2	7.31	0.22	792^3
Ma0.4	6.1	0.42	792^3
Ma0.6	6.47	0.61	792^3
Ma0.8	6.14	0.82	792^3

Table 4.2: Parameters of supersonic MHD simulation sets used. The Mach numbers in column "Model" are the initial values for the simulations. M_s and M_A are the instantaneous values at final snapshots. Resolution of the simulated cubes is 792^3.

cubes ($M_s \sim 7$, M_A ranges from 0.22 to 0.82, see Table 4.2) with resolution of 792^3, allow us to test our recipe more accurately.

In single fluid MHD simulations, we simulate three-dimensional velocity and density of the medium, as well as magnetic fields vectors. To predict dust distribution, we assume that it follows the simulated fluid. Note that our focus is to test the method on the simulations with well developed and characterized MHD turbulent cascade, rather than to model all the complexities of the ISM. Using the dust model given by Wardle & Konigl (1990), we can connect dust polarization with magnetic fields by computing Stokes parameters as

$$
\begin{aligned}
Q_{dust}(x,y) &= p' \int \rho(x,y,z) \; \frac{B_x^2 - B_y^2}{B_x^2 + B_y^2 + B_z^2} \; dz \; , \\
U_{dust}(x,y) &= p' \int \rho(x,y,z) \; \frac{2B_x B_y}{B_x^2 + B_y^2 + B_z^2} \; dz \; ,
\end{aligned}
\tag{4.1}
$$

where ρ is the density; B_x, B_y, B_z are magnetic field components, and it is assumed that individual dust grains have a fixed degree of polarization p'. Such

fixed value is not important if we consider only the orientation of polarization $\theta_{dust} = \frac{1}{2}\text{atan2}\,(U_{dust}, Q_{dust})$, as we do in this section. If we look in detail how Stokes parameters accumulate along the line of sight

$$Q_{dust}(x,y) = p' \int \rho(x,y,z)\ \cos 2\theta(x,y,z) \sin^2 \psi(x,y,z)\ dz\ ,$$

$$U_{dust}(x,y) = p' \int \rho(x,y,z)\ \sin 2\theta(x,y,z) \sin^2 \psi(x,y,z)\ dz\ ,$$

(4.2)

where θ is the local sky orientation angle and ψ is the angle with the line-of-sight of the magnetic field. We should note that p' represents the degree of polarization of emitted individual dust grains, which we assume to be a constant. Whereas, the observed degree of polarization, $p_{dust}(x,y) = \sqrt{Q_{dust}^2 + U_{dust}^2}$ will, in general, differ for different lines of sight.

As described in section 3, we put forward the modified version of VChG by imitating the addition process of Stokes parameters, and keeping velocity channel at their highest resolution. Hence, we expect a higher tracing precision of polarization when compared to the original VChG. To obtain a simple quantitative characterization of the angle difference $\Delta\phi$ between two maps covering the same region, we define the alignment measure (AM) as follow:[1]

$$AM = 2\ \langle \cos^2(\phi) - 1/2 \rangle \equiv \langle \cos 2\phi \rangle$$

(4.3)

where the ϕ is the angle difference between two vectors and averaging is done over the whole region. AM is a value ranging from -1 to 1, which provides us with an quantification of the overall alignment: AM=1 means perfect align-

---

[1]The alignment measure of this type was first introduced in González-Casanova & Lazarian (2017) and used in the subsequent papers. The alignment can be measured with this measure in respect to magnetic field or with polarization that acts as the proxy of the projected magnetic field. As we discussed earlier, due to the different properties of magnetic fields and polarization, as far as adding along the line of sight is concerned, the direction of the polarization obtained by the averaging along the line of sight may be different from the averaged along the line of sight direction of magnetic field. However, these differences are not important within our present discussion.

Figure 4.1: Comparison of tracing performance of the original VChG and the modified VChG in subsonic regime, for several Alfvénic Mach numbers. The blue segments show the simulated orientation of dust polarization, and the red segments show the orientation of dust polarization predicted by different VChGs. The parameters of simulations are from Table 4.1.

ment; AM=0 means no relationship; AM=-1 means two fields vector are perfectly perpendicular. Note that the measure does not distinguish between forward and backward pointings of the vectors, depending only on the axis of direction.

The comparison between synthetic polarization orientation and simulated polarization orientation is shown in Figure 4.1 (subsonic, $M_s \sim 0.9$) and Figure 4.2 (supersonic, $M_s \sim 7$). From these two figures, we can see that

1. AM of VChGs tend to decline with increasing M_A.

2. Tracing precision of the the pseudo-Stokes parameters based VChG (modified VChG) is improved versus the original version of VChG. For instance, in the subsonic case $AM > 0.8$ even for $M_A \sim 0.9$ while in supersonic case $AM > 0.8$ for $M_A < 0.6$. In the most challenging su-
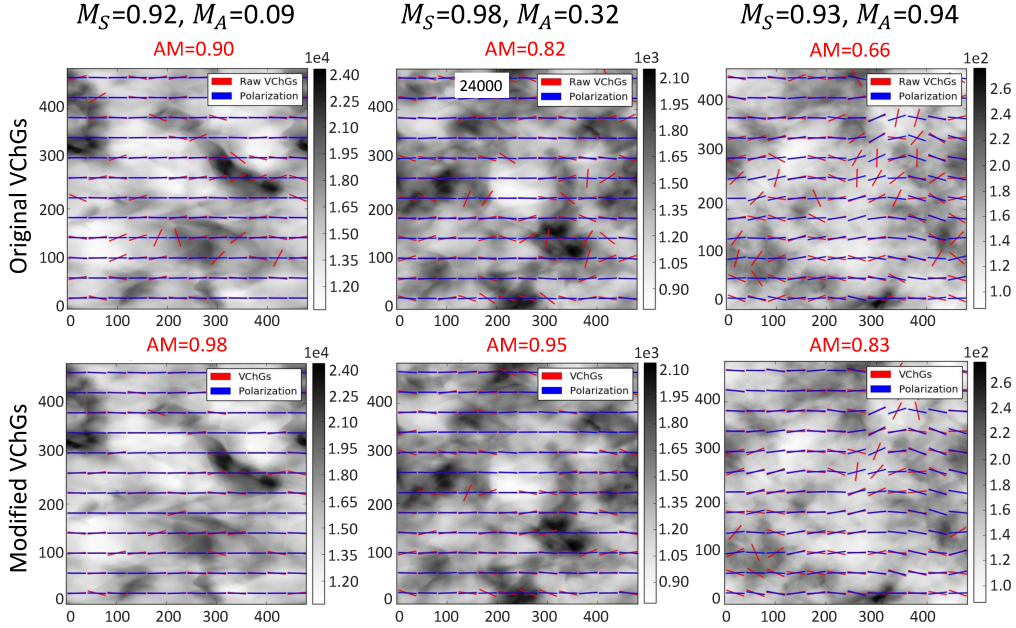
50
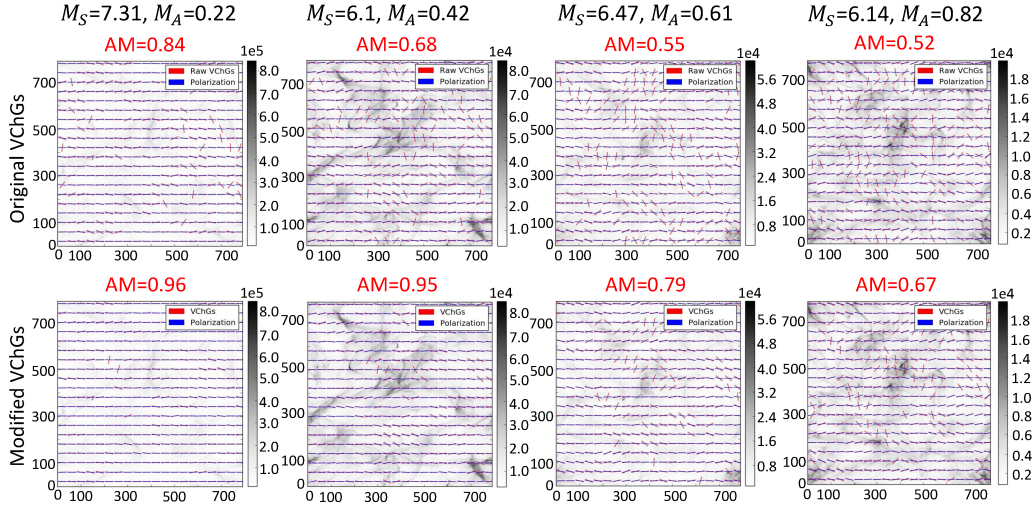
Figure 4.2: Comparison of tracing performance of the original VChG and the modified VChG in supersonic regime, for several Alfvénic Mach numbers. The blue vectors show the simulated orientation of dust polarization, and the red vectors show the orientation of dust polarization predicted by different VChGs. The parameters of simulations are from Table 4.2.

personic $M_A = 0.82$ case we still see an improvement from $AM \sim 0.5$ to $AM \sim 0.65$.

We also see that in some localized regions, the VChG directions deviate from or are even perpendicular to the simulated polarization directions. This is possibly because in those regions compressible magnetosonic modes dominate over Alfvénic modes, in which case velocity gradients are expected to be parallel rather than perpendicular to the magnetic field. These regions are the main contributors to the decrease of the alignment measure AM, which is a measure averaged over the whole field.

Note that since the original VChG did not predict degree of polarization, we only compare the orientation of polarization here. For orientation, the new version of VChG improves the tracing precision and works well in all sub-Alfvénic $M_A < 1$ regimes that were tested. These conclusions are robust in both subsonic and supersonic cases.

Chapter 5

Applying to observation

With the positive conclusions obtained in section 4, next we apply VChG to real observations. We produce the synthetic map of dust polarization from HI data in velocity channels, for which we use GALFA-HI DR2 (Peek et al., 2018). To test the accuracy of our synthetic map, we will compare it with the Planck's observed polarization at 353 GHz (Planck Collaboration et al., 2015).

5.1 Data overview

We use recently released HI data from GALFA-HI DR2 (The Galactic Arecibo L-band feed Array HI, see Peek et al. 2018), a survey of the 21 cm HI line over the Arecibo sky (decl. $1°17'$ to $+37°57'$ across all R.A.) with $\sim 3.5'$ FWHM beam resolution, 0.184 km/s spectral resolution ("Narrow" set), and with 352 mK median rms noise per 0.184 km/s channel. GALFA maps are produced with $1' \times 1'$ pixelization that somewhat oversamples the beam. For our analysis, we choose the sky region of GALFA-HI data whose right ascension (R.A.) ranges from $215.0°$ to $265.0°$ and declination (DEC.) ranges from $6.0°$ to $37.5°$, to avoid the regions near the Galactic plane and the North Galactic pole. Our region is similar to the field studied in Clark (2018) and two times larger in declination range to the field used for magnetic field comparison in Clark et al.

(2015). Following the steps described in chapter 3, we apply VChG to the PPV cubes of HI using 148 thin channels of 0.184 km/s width that span the velocity range from -13.6 km/s to 13.6 km/s, and apply a $1° \times 1°$ block averaging. The VChG angles and "degree of polarization" from HI data are calculated from Equations 3.10, 3.11.

As a comparison with the synthetic dust polarization, we plot the dust polarization observed by Planck mission. Since 353 GHz emission is dominated by the thermal dust, we use single frequency 353 GHz polarization map by PLANCK satellite to plot dust polarization (see Planck Collaboration et al. 2015). Using CMB-cleaned 353 GHz map or the component separated dust map, also provided by the Planck team, lead to no change in the conclusions.

Planck maps are provided in HEALPix[1] pixelization at $N_{side} = 2048$ which corresponds to approximately 1.7′ pixel linear size. The following processing is applied. Firstly, we smooth the observed Stokes parameters, I_{353}, Q_{353} and U_{353} by a Gaussian function with a 5′ FWHM. Secondly, to compare with GALFA-HI data, we transform the *Planck* Stokes parameters to Equatorial coordinates, and select the GALFA field. Thirdly, we re-bin Planck data using HEALPix provided interpolating functions onto a Cartesian grid with $1° \times 1°$ pixels, by averaging I_{353}, Q_{353} and U_{353} within the coarse pixels. The polarization angle θ_{353} and the degree of polarization p_{353} are then obtained by the usual relations to $I_{353}, Q_{353}, U_{353}$ (no de-biasing of p_{353} has been attempted to be consistent with our current treatment of the degree of polarization in the gradient method).

5.2 Results

The maps of polarization directions from VChG and Planck 353 GHz are shown in panel (a) and panel (b) in Figure 5.1 respectively. The orientation of the

---

[1]http://healpix.sourceforge.net
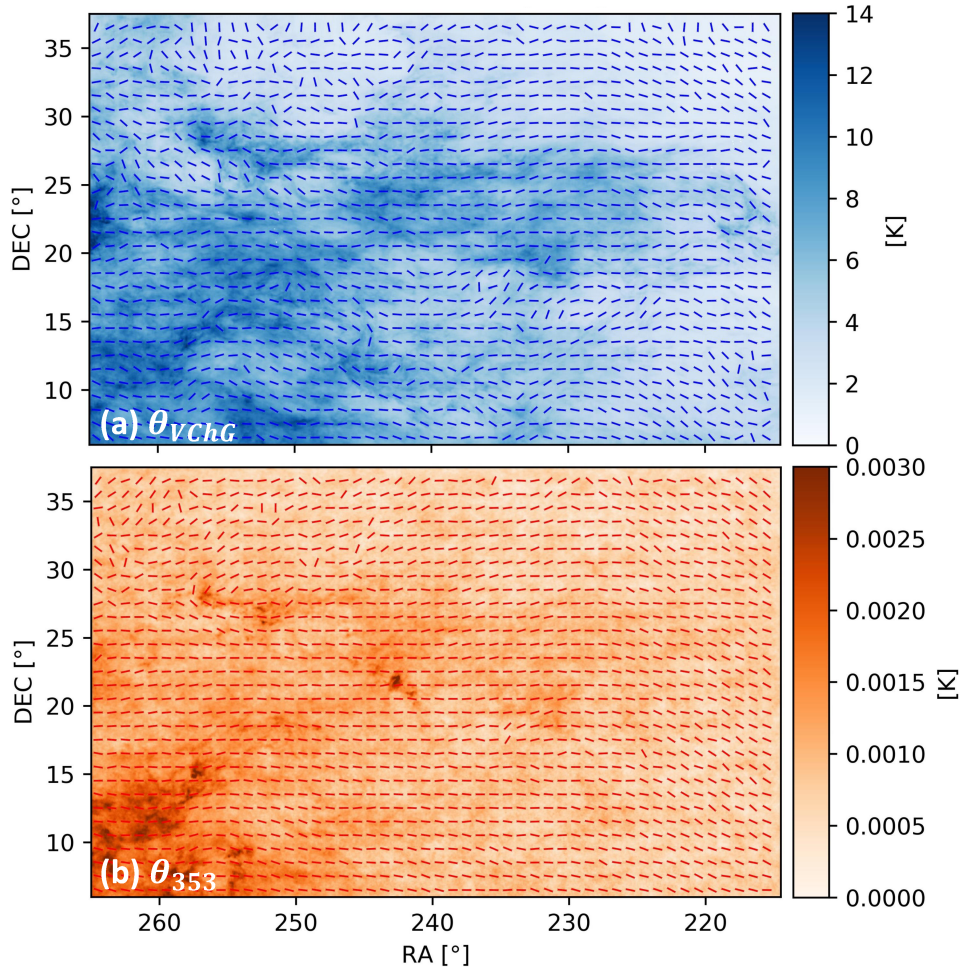
Figure 5.1: Polarization direction maps of the VChGs (panel (a)) and the Planck 353 GHz (panel (b)), where the background maps are the projected plane-of-sky intensity of GALFA-HI (blue) and Planck (orange). The VChG is calculated by GALFA-HI data with 0.184 km/s velocity channel width, ranging from -13.6 km/s to 13.6 km/s. Both the direction maps are pixelized at 1°; the background intensity maps are pixelized in their raw resolution of GALFA-HI and Planck.

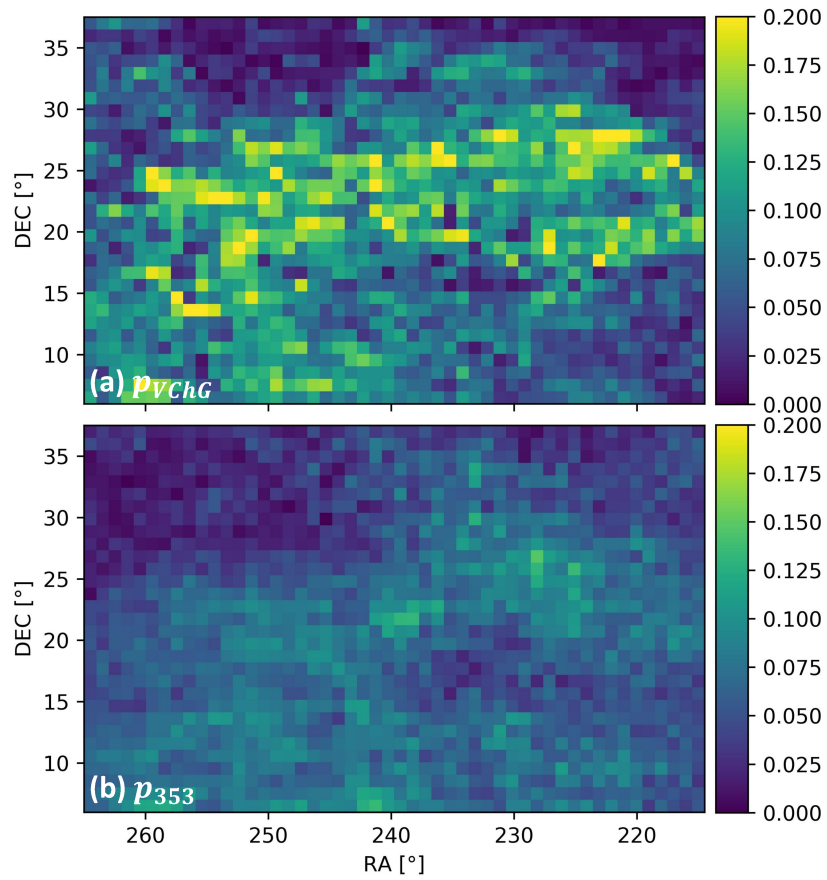Figure 5.2: Maps of the degree of polarization of the VChG (panel (a)) and the Planck 353 GHz (panel (b)), where the spatially mean values $\langle p_{VChG} \rangle = 0.082$ and $\langle p_{353} \rangle = 0.059$. Both maps are pixelized at $1°$.

line segments (here of equal length) shows the direction of the polarization; the background intensity maps show the projected plane-of-sky intensity of HI 21cm emission and Planck 353 GHz emission. The direction map allows us to visualize the underlying direction of the magnetic field. In the case of VChG, the surface brightness map is integrated along all velocity channels, so the gradients in individual channels that the VChG method is based upon are not explicitly the gradients of the intensity shown, though there is some correspondence.

In Figure 5.2, we show respectively the reconstruction of the degree of polarization by VChG in panel (a) and the degree of polarization map for Planck 353 GHz in panel (b). We see significant visual similarities in the structure of p maps. At the same time, VChG results give a level of polarization that is higher than the Planck data. This is expected, since in VChG we did not account for partial polarization level of individual dust grain emitters to begin with, as well as depolarization due to fluctuations of the magnetic field along the line of sight when the emission is collected in a channel from different physical depths. We note that simple constant scaling, e.g. with the ratio of the spatial means of two maps $\langle p_{VChG} \rangle / \langle p_{353} \rangle \approx 1.4$, is insufficient to explain all the differences. This points to the necessity to model variation of polarization degrees p_i between individual lines-of-site to achieve better correspondence. The gradient technique advanced in this paper has advantage of being able to easily incorporate such models by assigning Stokes parameters to fine-grain pixels, with local direction given by the gradient as before, but using non-uniform $p_p(i,j)$ before combining the data into coarse-grained $\widetilde{Q}_B, \widetilde{U}_B$.

Let us now turn to the quantitative comparison between two datasets. In Figure 5.3 we compare only the directional information. The top panel overlays the two maps from Figure 5.1 to see the matching and the differences in pixel to pixel direction of polarization, while the bottom panel is the explicit map of angle difference measure $\cos 2(\theta_{VchG} - \theta_{353})$. We see that over most pixels of
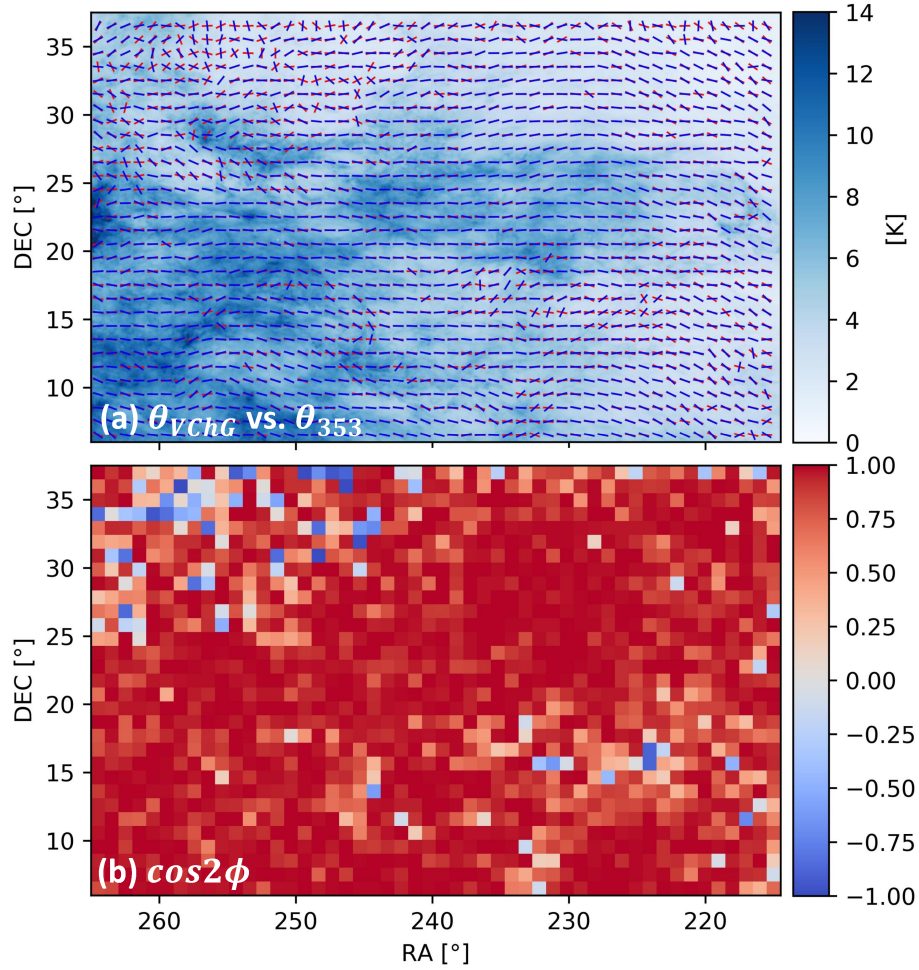
Figure 5.3: The panel (a) shows the pixel-by-pixel comparison between θ_{VChG} (blue) and θ_{353} (red), where the background intensity map is the projected HI intensity. The panel (b) shows the spatial distribution of $cos2\phi$, whose spatially mean value $AM = 0.77$. Note that ϕ is the angle difference between θ_{353} and θ_{VChG}. Both maps are pixelized at 1°.
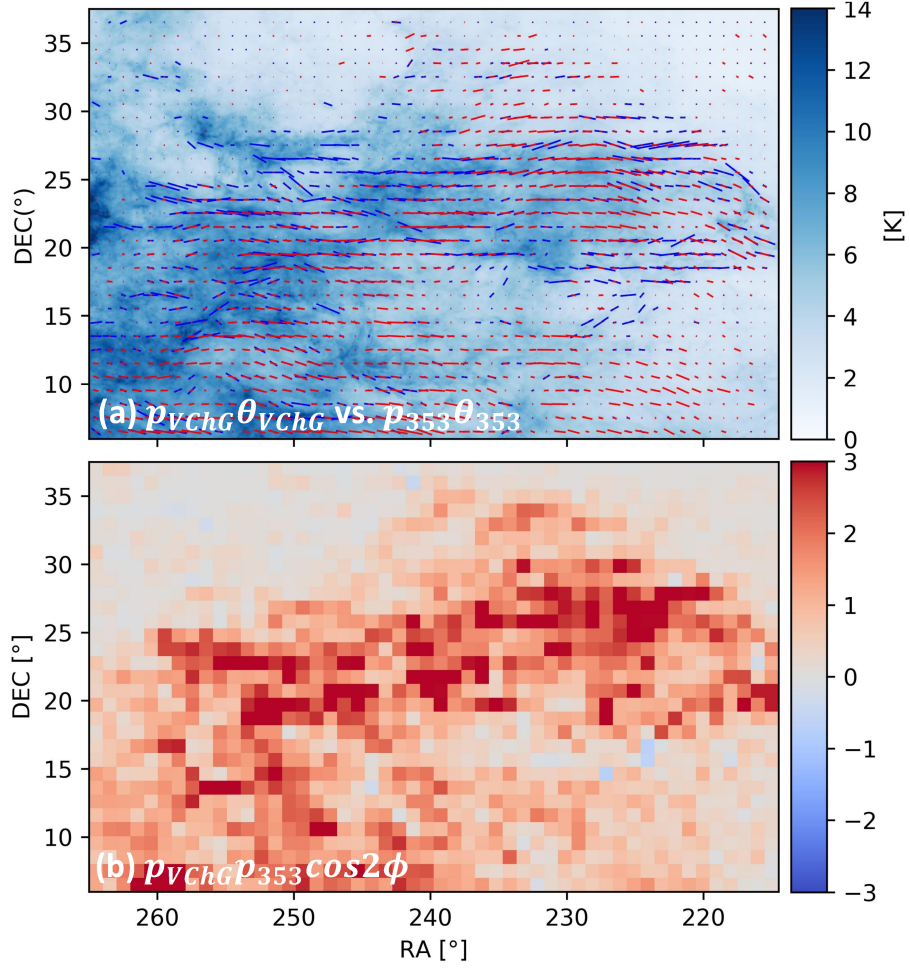
Figure 5.4: The panel (a) shows the pixel-by-pixel comparison between $p_{VChG}\theta_{VChG}/\langle p_{VChG} \rangle$ (blue) and $p_{353}\theta_{353}/\langle p_{353} \rangle$ (red), where the background intensity is the projected HI intensity map. The panel (b) shows the map of $p_{VChG}p_{353}cos2\phi/\langle p_{VChG}p_{353} \rangle$, whose spatially mean value $ppAM = 0.89$. Note that ϕ is the angle difference between θ_{353} and θ_{VChG}. Both maps are pixelized at $1°$.

the map this measure is close to unity, indicating a high degree of alignment. Indeed, the average of the whole map value is the earlier introduced $AM = \langle \cos 2\phi \rangle$, where $\phi = \theta_{353} - \theta_{VChG}$. We obtain $AM = 0.77$ for VChG as compared to Planck 353 GHz. This level of accuracy of reconstructing the direction from HI data is on par with the best results quoted in the literature, e.g. Lazarian & Yuen (2018a), despite the much larger area studied and simplicity of our approach. Clark et al. (2015) and Clark (2018) do not quote the AM parameter explicitly but the authors made available their $I_{RHT}, Q_{RHT}, U_{RHT}$ reconstructed maps in GALFA-HI archive[2]. So for quantitative comparison we have performed the alignment measurement from these RHT data ourselves. We have followed the pipeline described in Clark (2018) to obtain channel-added Q_{HI}, U_{HI} over exactly the same patch of the sky as in this paper, with two modifications to match parameters of our reconstruction, namely, restricting the velocity range to ± 13.6 km/s (since RHT Stokes parameters are provided in 3.68 km/s wide channels, we have used 7 RHT channels that cover -12.9 km/s to $+12.9$ km/s) and averaging resulting Stokes parameters over $1°$ square super-pixels as in our analysis, instead of larger $90'$ FWHM Gaussian smoothing suggested in Clark (2018). We have obtained $AM = 0.76$ for the comparison of these RHT maps with Planck maps as the result.[3] For visual comparison of the two techniques, the synthetic map of polarization directions from RHT is shown alongside VChG in Appendix Figure A.1.

The AM alignment measure mostly reflects the variance of angle difference between two maps. Indeed, at least at small angle differences $\langle \cos 2\phi \rangle \approx 1 + \langle \phi^2 \rangle /2$. It is also instructive to consider an associate measure, $sAM = \langle \sin 2\phi \rangle$, which, in contrast, reflects the systematic mean deviation of directions in one map versus another (this measure will vanish if two maps are perfectly aligned

---

[2] https://purcell.ssl.berkeley.edu/RHT.php

[3] As another reference point, Clark & Hensley (2019) quotes $AM = 0.71$ for a full-sky comparison between their RHT analysis of HI 4π Survey (HI4PI Collaboration et al. 2016) and Planck 353 GHz directions.

or if the angle difference has equal probability to be of opposite signs. It is equal to maximum $+1$ if one map direction is $\pi/4$ above the other and -1 if it is $\pi/4$ below). The pixel map of this quantity is difficult to interpret, in particular because pixels with near perpendicular directions give equally low value to ones with parallel alignment, so we do not present it here. However, the overall average in our comparison is $sAM = 3.3 \times 10^{-2}$, which indicates lack of systematic angular deviation.

To include the full polarization information in our quantitative comparison, we evaluate the correlation between Planck's polarization map and synthetic polarization map using the cross-correlation function of complex polarization $P = Q + iU$ at zero lag, whose pixel by pixel estimator is

$$
\begin{aligned}
\xi(\mathbf{X}) &\equiv P_{353}(\mathbf{X}) \; P^*_{VChG}(\mathbf{X}) \\
&= Q_{353}Q_{VChG} + U_{353}U_{VChG} \\
&\quad + i\left(U_{353}Q_{VChG} - Q_{353}U_{VChG}\right)
\end{aligned}
\tag{5.1}
$$

Divided by the intensities $I_{353}I_{VChG}$, we can interpret the correlation function as

$$
\frac{\xi}{I_{353}I_{VChG}} = p_{353}p_{VChG}\cos 2\phi + ip_{353}p_{VChG}\sin 2\phi
\tag{5.2}
$$

Therefore, the real part of ξ measures the alignment between Planck's orientation and synthetic orientation weighted by the product of degrees of polarization $p_{353}p_{VChG}$. Taking the overall average and further normalizing the weights we can define a polarization degree weighted alignment measure as

$$
ppAM = \frac{\langle p_{353}p_{VChG}\cos 2\phi\rangle}{\langle p_{353}p_{VChG}\rangle}
\tag{5.3}
$$

Here $ppAM$ also varies from -1 to 1, with main difference from AM is that $ppAM$ focuses more on the regions with higher degree of polarization. Then, we are able to quantitatively compare the polarized direction maps between two

60

datasets. As shown in Figure 5.4, the panel (a) overlaps the polarized vectors of VChG and Planck 353GHz, where the vectors are weighed by its degree of polarization; more polarized it is, longer the vectors will be. The panel (b) shows the spatial distribution of $p_{VChG}p_{353}cos2\phi/\langle p_{VChG}p_{353}\rangle$, whose average value $ppAM = 0.89$. A higher value of $ppAM$ than AM indicates that our VChG method traces the real polarization better in more polarized regions. This is not surprising, since high degree of polarization also reflects the low variance in gradient directions, and thus lower uncertainty in determining the polarization direction within the coarse-grained pixel block. Therefore, from another point of view, ppAM can be considered as an alignment measure where angle differences are weighted by their inverse uncertainty. Similarly, we can evaluate the imaginary part of the correlation function, $\langle p_{VChG}p_{353}\sin 2\phi\rangle/\langle p_{VChG}p_{353}\rangle$, which equals 5.7×10^{-3}, which again points to the lack of systematic misalignment.

To inspect the correlation between the Planck dust polarization map and the VChG synthetic dust polarization map from another perspective, we plot the two-dimensional histograms between them in Figure 5.5, for the degree of polarization in panel (a) and for the orientation of polarization in panel (b). For the degree of polarization, we can see a good correlation between p_{353} and p_{VChG}. To quantify the systematic deviation of our estimation, we linearly fit the scatter using a one-parameter model, $p_{VChG} = ap_{353}$. As shown in the panel (a), the result given by least orthogonal distance square fitting is $p_{VChG} = 1.6p_{353}$, and the Pearson's correlation coefficient is $r = 0.51$. Following the same steps as described in the polarization orientation reconstruction, we reconstruct the synthetic map of degree of polarization using RHT, t_{HI}, and obtained the linear fitting $t_{HI} = 3.5p_{353}$, with Pearson's correlation coefficient $r = 0.53$[4]. As a reference, the synthetic map of degree of polarization from

---

[4] In Clark (2018), the linear fit $t_{HI} = 2.1p_{353} + 0.049$ and the correlation coefficient $r \sim 0.7$ have been obtained, which is different from the RHT fitting results that we give here. These values, however, were obtained using different and/or additional steps to process the
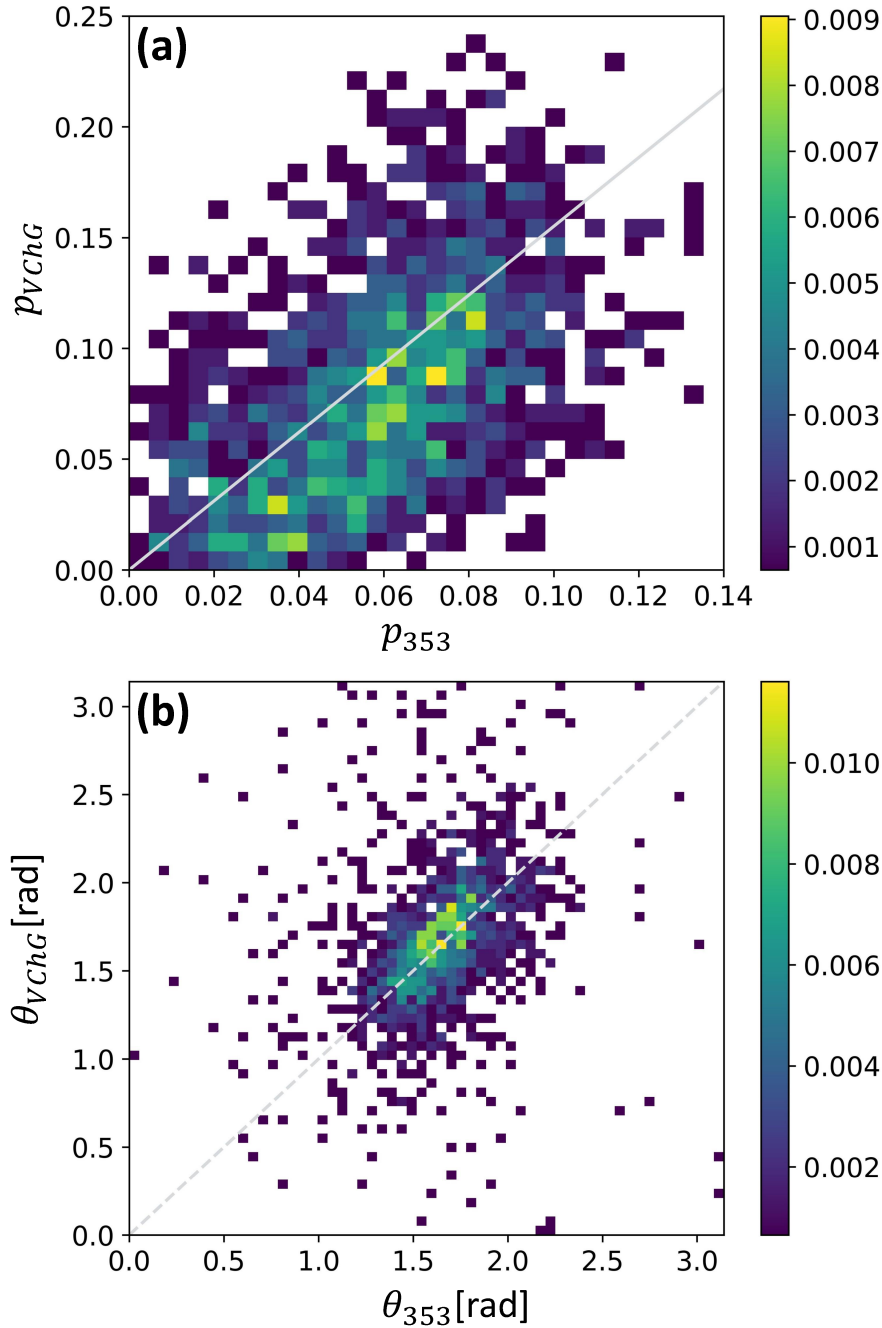
Figure 5.5: The panel (a) shows the two-dimensional histogram of the degree of polarization between Planck 353 GHz (p_{353}) and VChG (p_{VChG}), where the grey solid line, $p_{VChG} = 1.6 p_{353}$, is the least orthogonal distance square fitting of their scatters. The panel (b) shows the two-dimensional histogram of the polarization orientation of VChG (θ_{VChG}) and Planck 353 GHz (θ_{353}). The dashed line is a reference line $\theta_{VChG} = \theta_{353}$, along which the alignment is perfect. Both histograms are normalized by the total count.

RHT is provided in Appendix Figure A.2. In comparison, we can find that 1) the VChG method has the similar level correlation coefficient r as the RHT method, which, combining the results of alignment measures, indicates that quantitatively the two methods have similar reconstruction of the synthetic dust polarization maps; 2) the RHT's prediction of degree of polarization is more than three times of that of the Planck, and two times that of our VChG approach. We have tested the effect of channel thickness by computing p_{VChG} in the synthetic velocity channels of the same thickness as the RHT (3.68 km/s). We find that in such thicker channels p_{VChG} increases by a factor ~ 1.2, which is, however, still not sufficient to explain the difference of 2 times between t_{HI} and p_{VChG}. This confirms that RHT misses some sources of depolarization that VChG includes.

For the orientation of polarization, as shown in panel (b) of Figure 5.5, we can also see a good correlation between θ_{353} and θ_{VChG}. If the two angles are statistically equal to each other, i.e. $\theta_{VChG} \approx \theta_{353}$, we expect their relation to be described by a line starting from the origin with slope equalling one. We can see that the grey dashed line indeed well matches the histogram.

---

final maps relative to this paper. In Clark (2018), different sky regions were used; larger Gaussian smoothing with kernel FWHM = $90'$ instead of rebinning in $1°$ square super-pixels was applied; and, importantly, pixels that have a signal-to-noise ratio $SNR < 2$ in p_{353} measurements at the 90% confidence level were masked, while in this paper all the pixels have been used. We also point out that simple fitting results of a scatter plot with positively defined data must be treated with caution. For instance, if a linear fit allows for a varying intercept and is obtained by minimizing orthogonal distances, some data points may be compared with "unphysical" counterparts on the fitted line with negative values of either p_{353} or p_{VChG}. On the other hand, a standard linear fitting that minimizes vertical separation gives non-symmetric result when applied to $p_{VChG}(p_{353})$ or the inverse, $p_{353}(p_{VChG})$.

Chapter 6

Discussion

6.1 Limitations and Applicability

Our present study is the first study exploring the applicability of the VChG to predict dust polarization. The modifications to original VChG suggests an increasingly good correspondence with Planck 353 GHz dust map. At the same time, at the current stage, the VChG also has several differences from real dust model, as well as some limitations.

First of all, our current model does not account to full extent for three dimensional orientation of the magnetic field along the line of sight. If we look back to the real dust model (Equation 4.2), we can see that the accumulation of Stokes parameters depends not only on the plane-of-sky orientation of magnetic field, θ, but also the line-of-sight orientation of the magnetic field. More specifically, it depends on the angle difference between line-of-sight magnetic field with the plane-of-sky, the $\sin^2 \psi$ term in formula. In our VChG method, by measuring the gradient of HI intensity on the sky, we could only predict, statistically, the projected plane-of-sky orientation of magnetic field, i.e U/Q of Equation 4.2, but not the degree of polarization along an individual line of sight nor, even more importantly, its fluctuations between the lines-of-sight. Such incompleteness decreases the accuracy of synthetic dust map. Improvements

call for better studies of the three dimensional magnetic field distribution. We address this issue in the forthcoming publications.

Our model of polarization arising from aligned dust can also be improved. We assumed perfect alignment of silicate dust, which is a reasonable assumption for the radiative torque (RAT) alignment of dust grains in diffuse regions (see Lazarian & Hoang 2007b; Andersson et al. 2015). This have direct relevance to the issue of the normalization of parameter p. The issue of constant temperature of dust that we assumed seems to be more controversial and it requires more study. We treat this as only first approximation to the complex problem that we address.

At this moment, our maps can be used as a prior for removing the foreground polarization from dust. This use of HI was suggested in Clark et al. (2015) and Clark (2018). Similar to Clark's idea, we can estimate the change of the degree of polarization. However, a big difference between our approach and that in Clark (2018) is that we use the distribution of directions within subblocks, rather than just the change of the direction of the filaments measured in different channel maps. In this sense, our approach provides more statistical information, which gives a potential to further improve our estimates of polarization.

We note that the VChG method, fundamentally, relies just on the direction-sensitive statistics of intensity (here the gradients, but more generally, the two-point directional structure function, see section 2.3) to track the direction of the magnetic field. In turbulent medium, this is theoretically expected not only for PPV channel maps, but also for velocity centroids as well as signals of different nature such as the synchrotron emission, to which the gradient technique can also be applied. In particular, the gradient technique is agnostic to the interpretation of structures in PPV space and bypasses the discussion of the relative role of real space density inhomogeneities and velocity mapping in channel maps (Clark et al., 2019), working well with both structures created

65

by velocities and densities (see Hu et al. 2019b).

The studies in Kandel et al. (2016) suggest that the Alfvén Mach number corresponding to the high latitude dust is smaller than unity. This helps to our analysis, as the VChG for low M_A works better and does not require additional spatial filtering of low spacial frequencies (see Lazarian & Yuen 2018a).

6.2 Dealing with Noise

Every observational data maps contain noise contribution which affect the analysis. If we are able to know the noise field $\boldsymbol{N}(\boldsymbol{X})$ of the observed HI intensity, similar as Equation 3.1, we are able to calculate the gradient along x and y direction of the noise

$$N_x = \nabla_x \boldsymbol{N}(\boldsymbol{X}) = \frac{1}{2}[\boldsymbol{N}(x+2, y) - \boldsymbol{N}(x, y)] \tag{6.1}$$

$$N_y = \nabla_x \boldsymbol{N}(\boldsymbol{X}) = \frac{1}{2}[\boldsymbol{N}(x, y+2) - \boldsymbol{N}(x, y)] , \tag{6.2}$$

where the noise mostly varies across different pointed sky regions $\boldsymbol{X}$. Along different velocity channels, the noise can be approximately treated as the same. The covariance matrix of noise gradient at a given point can be calculated by

$$\begin{bmatrix} \sigma_{N_{xx}} & \sigma_{N_{xy}} \\ \sigma_{N_{xy}} & \sigma_{N_{yy}} \end{bmatrix} = \begin{bmatrix} < N_x^2 > & < N_x N_y > \\ < N_x N_y > & < N_y^2 > \end{bmatrix} . \tag{6.3}$$

Therefore, assuming that the noise is not correlated with the signal, we are able to deduct the noise from calculated covariance matrix

$$\begin{bmatrix} \sigma'_{xx} & \sigma'_{xy} \\ \sigma'_{xy} & \sigma'_{yy} \end{bmatrix} = \begin{bmatrix} \sigma_{xx} - \sigma_{Nxx} & \sigma_{xy} - \sigma_{Nxy} \\ \sigma_{xy} - \sigma_{Nxy} & \sigma_{yy} - \sigma_{Nyy} \end{bmatrix} . \tag{6.4}$$

Theoretically, after the noise covariance deduction, we are able to obtain a more realistic value of degree of polarization, especially when the noise-to-signal ra-

tio is relatively high. As noted in Equation 3.19, when the observational noise field $\boldsymbol{N}(\boldsymbol{X})$ is isotropic, or in one-point covariance matrix of its gradients the cross terms are small compared with diagonal terms, the noise will not influence the gradient angle in coarse grain, θ_B. Hence we mainly care about the the noise's influence of the value of degree of polarization, p_B. To quantitatively test noise's influence and the effect of noise correction, we numerically add variable level of Gaussian noise to a MHD simulation data. For this test we did not perform the full (expensive) MHD simulation runs, but simply generated Gaussian realizations of the linear MHD modes with anisotropic power spectrum of the magnetic field. The velocity channel maps were then constructed assuming the uniform density of HI, but velocity reflecting MHD motions. The noise was then superimposed on the the channel maps, at the level controlled by noise-to-signal ratio, which is the ratio of noise's standard deviation to simulated plasma's intensity. This simplified setup allows us to cheaply modify the signal parameters. Here we present the results for strong incompressible turbulence where Alfvén and slow modes are both divergence free and have an equal power.

Histograms of p_B calculated with different level of noise are shown in Figure 6.1. We can see that when the noise level is relatively low (noise-to-signal ratio < 0.01), distribution of p_B is not obviously affected; while when the noise level becomes relatively high (noise-to-signal ratio > 0.01), p_B significantly decreases. Using our covariance method, histograms of the noise-corrected degree of polarization p'_B with corresponding noise level are shown in Figure 6.2. We can see that even though the intensity field is added with different level of noise, the corrected p'_B keeps almost the same mean value as that without noise, which numerically supports the feasibility of covariance noise-correction method. Naturally, as a trade-off, standard deviation of p'_B will increase with higher level of noise. More clearly, we show the change of mean value and standard deviation of p_B as well as p'_B in different noise-to-signal ratio, which

Figure 6.1: Histograms of p_B with different noise-to-signal ratio (the "std_factor" in the plot). The noise-to-signal controls the level of Gaussian noise added to the simulated MHD channel maps.
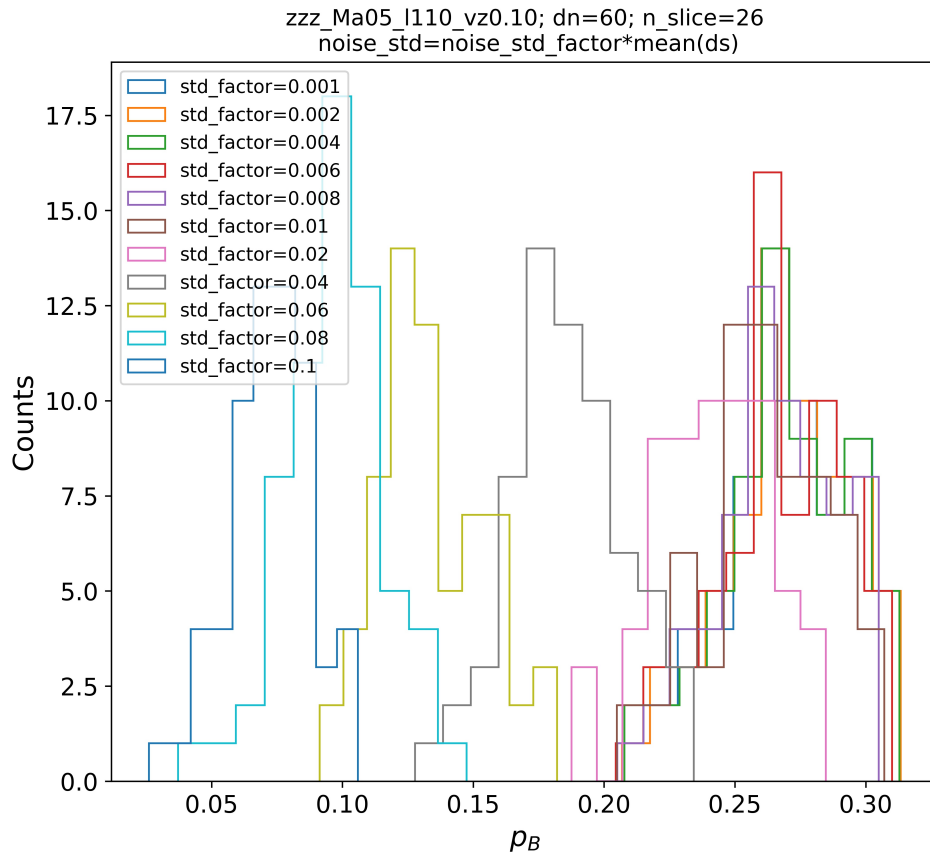
Figure 6.2: Histograms of p'_B with different noise-to-signal ratio (the "std_factor" in the plot). The noise-to-signal controls the level of Gaussian noise added to the simulated MHD channel maps.
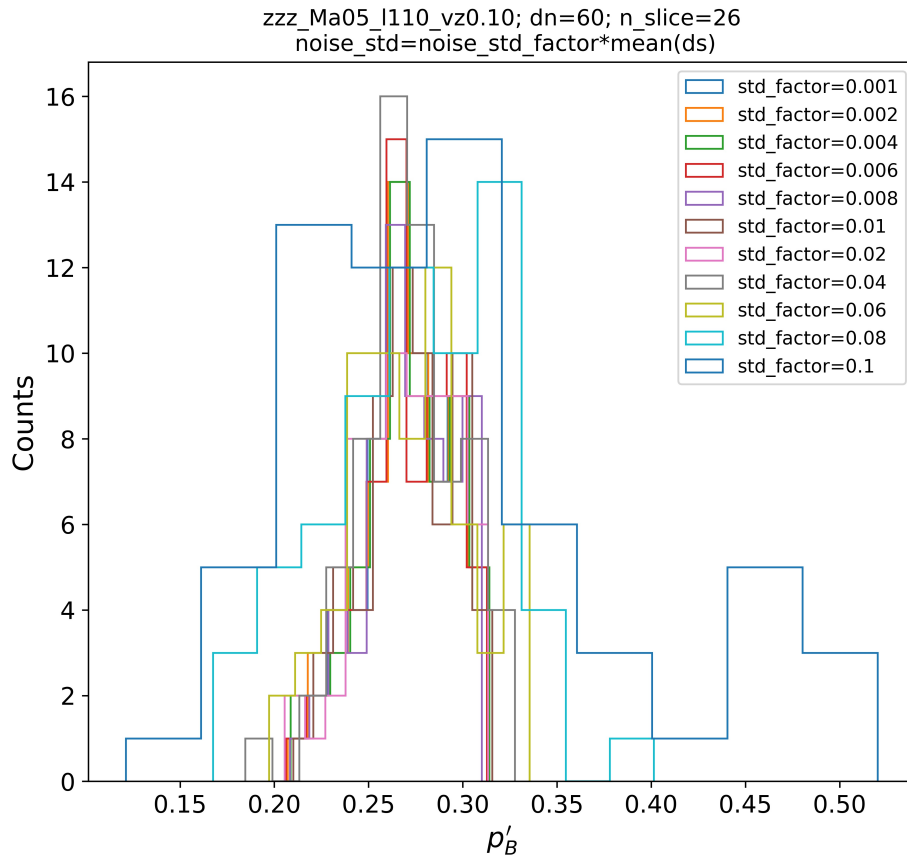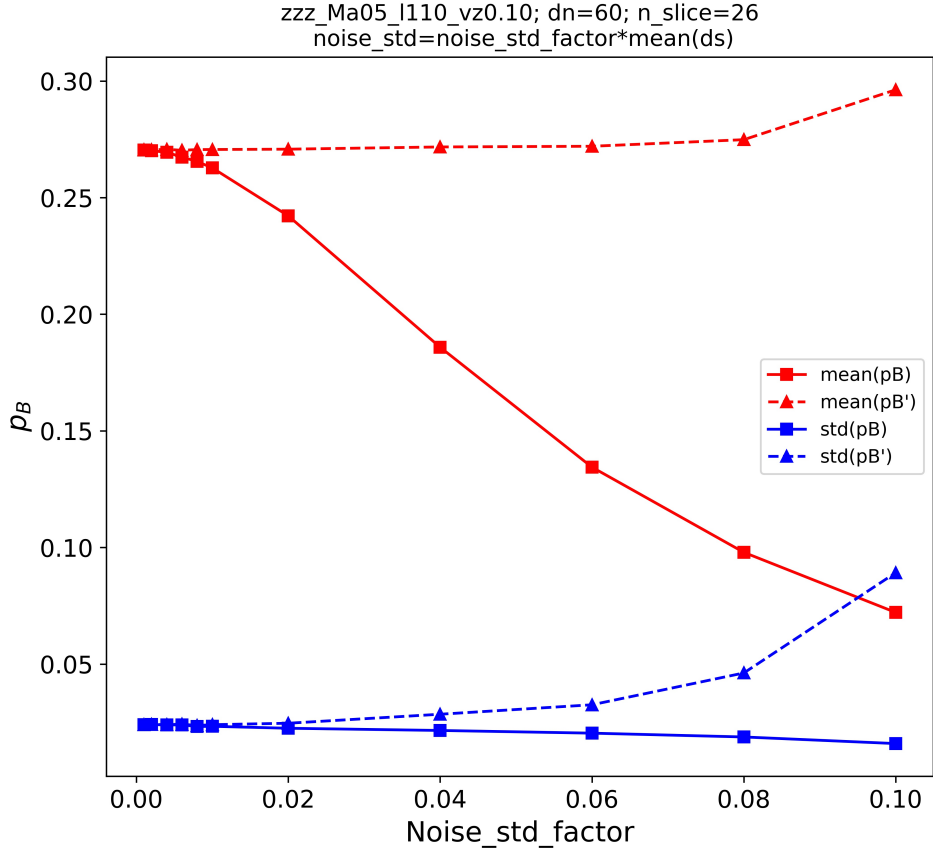
Figure 6.3: Changes of mean and standard deviation of p_B and p'_B with different noise-to-signal ratio (the "Noise_std_factor" in the plot). The noise-to-signal controls the level of Gaussian noise added to the simulated MHD field.

supports that, with higher noise level, the p_B will significantly decrease but the p'_B will almost keep the same. This plot also guides quantitatively us the influence of noise. Namely, if the observation quality of HI is high (noise-to-signal ratio < 0.01), the influence of noise is not obvious and thus there is no need to correct the noise; while if the observation quality of HI is not that ideal (noise-to-signal ratio > 0.01), it will be practical and beneficial to correct the degree of polarization using the covariance method.

Thereafter, in our case, the question becomes what is the noise level of HI data. The exact observational noise distribution of HI is anisotropic and decided by many factors, which will be studied in our future work. Nevertheless,

here, it would be illuminating to estimate the level of noise-to-signal ratio of GALFA-HI data. Peek et al. (2018) mentions that the rms noise of GALFA-HI data in 0.184 km s^{-1} resolution is 352 mK. At our studied region, the mean intensity of the central velocity channel (0 km s^{-1}) of is ~ 10 K. Combining the two numbers, the magnitude of noise-to-signal ratio of GALFA-HI data can be estimated as ~ 0.035, which is larger than our aforementioned threshold 0.01. Revisiting Figure 6.3, we see that noise-to-signal 0.035 value would give $p_B \sim 0.7 p'_B$, which would be a significant underestimation if the noise effect is not corrected. Therefore, from this rough but illuminating estimation, for GALFA-HI data in our studied region, the noise covariance will largely correct the value of degree of polarization.

Chapter 7

Conclusion

In this thesis, by constructing pseudo-Stokes parameters and analytically studying the gradient statistics, we improve the VChG technique originally put forward by Lazarian & Yuen (2018a). By using the direction sensitive statistics such as gradients of channel intensities, we demonstrate that HI is a promising tool to map polarized dust foregrounds and study magnetic field and turbulence in Galaxy. We apply the VChG method to the GALFA-HI data in sky region with R.A. $215.0° - 265.0°$ and DEC. $6.0° - 37.5°$ and successfully produce synthetic maps of dust polarization, both orientation and degree of polarization. To summarize, we have reached the following conclusions.

- Adding up the pseudo-Stokes parameters within the VChG technique improves tracing accuracy of polarization orientation compared to its original version. Such improvement is confirmed in numerical MHD simulation with different magnetization. In the observational region that we study, a high AM 0.77 is given between the synthetic dust polarization orientation and Planck 353 GHz dust polarization orientation.

- Making use of the pseudo-Stokes parameters, the new modification of VChG technique makes it possible to predict degree of dust polarization, which shows a good correspondence with real 353 GHz dust map, with

Pearson's correlation coefficient $r = 0.51$. Such coefficient is comparable to previous study.

- By assuming Gaussian distribution of linear gradient of the HI field, we successfully give theoretical description of the local gradient angle's statistics, which well fits the statistics of real HI data.

- Thanks to the theoretical description of local gradient angle distribution, we have demonstrated how to incorporate noise information into VChG analysis by subtracting noise gradient's covariance. We demonstrate in numerical MHD simulations that mean value of the covariance-corrected degree of polarization p'_B almost is not influenced by noise added. After an order of magnitude estimation of GALFA-HI's noise level, we show that the noise correction method would significantly fix the value of synthetic degree of polarization, which is a promising direction for our future study.

Bibliography

Abbott B. P., et al., 2016a. Observation of gravitational waves from a binary black hole merger, Phys. Rev. Lett., 116, 061102

Abbott B. P., et al., 2016b. Gw151226: Observation of gravitational waves from a 22-solar-mass binary black hole coalescence, Phys. Rev. Lett., 116, 241103

Abbott B. P., et al., 2017a. Upper limits on the stochastic gravitational-wave background from advanced ligo's first observing run, Phys. Rev. Lett., 118, 121101

Abbott B. P., et al., 2017b. Gw170104: Observation of a 50-solar-mass binary black hole coalescence at redshift 0.2, Phys. Rev. Lett., 118, 221101

Abbott B. P., et al., 2017c. Gw170814: A three-detector observation of gravitational waves from a binary black hole coalescence, Phys. Rev. Lett., 119, 141101

Abbott B. P., et al., 2017d. Gw170817: Observation of gravitational waves from a binary neutron star inspiral, Phys. Rev. Lett., 119, 161101

Ade P. A. R., et al., 2014. Detection of b-mode polarization at degree angular scales by bicep2, Phys. Rev. Lett., 112, 241101

Ade P. A. R., et al., 2015. Joint analysis of bicep2/keck array and planck data, Phys. Rev. Lett., 114, 101301

Alfvén H., 1942. Existence of Electromagnetic-Hydrodynamic Waves, Nature, 150, 405

Andersson B. G., Lazarian A., Vaillancourt J. E., 2015. Interstellar Dust Grain Alignment, ARA&A, 53, 501

Armstrong J. W., Rickett B. J., Spangler S. R., 1995. Electron Density Power Spectrum in the Local Interstellar Medium, ApJ, 443, 209

Balbi A., et al., 2001. Erratum: Constraints on Cosmological Parameters from MAXIMA-1, ApJ, 558, L145

Barkats D., et al., 2014. DEGREE-SCALE COSMIC MICROWAVE BACK-GROUND POLARIZATION MEASUREMENTS FROM THREE YEARS OF BICEP1 DATA, The Astrophysical Journal, 783, 67

Barnett S. J., 1935. Gyromagnetic and electron-inertia effects, Rev. Mod. Phys., 7, 129

Bennett C. L., et al., 2003. First-Year Wilkinson Microwave Anisotropy Probe (WMAP) Observations: Preliminary Maps and Basic Results, ApJS, 148, 1

Bischoff C., et al., 2008. New measurements of fine-scale CMB polarization power spectra from CAPMAP at both 40 and 90 GHz, The Astrophysical Journal, 684, 771

Boulanger F., Perault M., 1988. Diffuse Infrared Emission from the Galaxy. I. Solar Neighborhood, ApJ, 330, 964

Boulanger F., Abergel A., Bernard J. P., Burton W. B., Desert F. X., Hartmann D., Lagache G., Puget J. L., 1996. The dust/gas correlation at high Galactic latitude., A&A, 312, 256

Bradt H., 2014, Astrophysics Processes

Brandenburg A., Lazarian A., 2013. Astrophysical Hydromagnetic Turbulence, Space Sci. Rev., 178, 163

Caldwell R. R., Hirata C., Kamionkowski M., 2017. Dust-polarization Maps and Interstellar Turbulence, ApJ, 839, 91

Callen J., 2006, Fundamentals of Plasma Physics

Challinor A., Peiris H., 2009, in Novello M., Perez S., eds, American Institute of Physics Conference Series Vol. 1132, American Institute of Physics Conference Series. pp 86–140 (arXiv:0903.5158), doi:10.1063/1.3151849

Chen F. F., 2016, Introduction to Plasma Physics and Controlled Fusion, doi:10.1007/978-3-319-22309-4.

Chepurnov A., Lazarian A., 2010. Extending the Big Power Law in the Sky with Turbulence Spectra from Wisconsin Hα Mapper Data, ApJ, 710, 853

Cho J., Vishniac E. T., 2000. The Anisotropy of Magnetohydrodynamic Alfvénic Turbulence, ApJ, 539, 273

Cho J., Lazarian A., Vishniac E. T., 2002. Simulations of Magnetohydrodynamic Turbulence in a Strongly Magnetized Medium, ApJ, 564, 291

Clark S. E., 2018. A New Probe of Line-of-sight Magnetic Field Tangling, ApJ, 857, L10

Clark S. E., Hensley B. S., 2019. Mapping the Magnetic Interstellar Medium in Three Dimensions over the Full Sky with Neutral Hydrogen, ApJ, 887, 136

Clark S. E., Hill J. C., Peek J. E. G., Putman M. E., Babler B. L., 2015. Neutral Hydrogen Structures Trace Dust Polarization Angle: Implications for Cosmic Microwave Background Foregrounds, Physical Review Letters, 115, 241302

Clark S. E., Peek J. E. G., Miville-Deschênes M. A., 2019. The Physical Nature of Neutral Hydrogen Intensity Structure, ApJ, 874, 171

Crutcher R. M., 1999. Magnetic Fields in Molecular Clouds: Observations Confront Theory, ApJ, 520, 706

Crutcher R. M., Wandelt B., Heiles C., Falgarone E., Troland T. H., 2010. Magnetic Fields in Interstellar Clouds from Zeeman Observations: Inference of Total Field Strengths by Bayesian Analysis, ApJ, 725, 466

Cudlip W., Furniss I., King K. J., Jennings R. E., 1982. Far infrared polarimetry of W51A and M42, MNRAS, 200, 1169

Davis Leverett J., Greenstein J. L., 1951. The Polarization of Starlight by Aligned Dust Grains., ApJ, 114, 206

Dolginov A. Z., Mitrofanov I. G., 1976. Orientation of Cosmic Dust Grains, Ap&SS, 43, 291

Draine B. T., 2011, Physics of the Interstellar and Intergalactic Medium

Draine B. T., Lazarian A., 1998. Diffuse Galactic Emission from Spinning Dust Grains, ApJ, 494, L19

Draine B. T., Weingartner J. C., 1996. Radiative Torques on Interstellar Grains. I. Superthermal Spin-up, ApJ, 470, 551

Elmegreen B. G., Scalo J., 2004. Interstellar Turbulence I: Observations and Processes, ARA&A, 42, 211

Erickson W. C., 1957. A Mechanism of Non-Thermal Radio-Noise Origin., ApJ, 126, 480

Ewen H. I., Purcell E. M., 1951. Observation of a Line in the Galactic Radio Spectrum: Radiation from Galactic Hydrogen at 1,420 Mc./sec., Nature, 168, 356

Gold T., 1952. The alignment of galactic dust, MNRAS, 112, 215

Goldreich P., Sridhar S., 1995. Toward a theory of interstellar turbulence. 2: Strong alfvenic turbulence, ApJ, 438, 763

González-Casanova D. F., Lazarian A., 2017. Velocity Gradients as a Tracer for Magnetic Fields, ApJ, 835, 41

González-Casanova D. F., Lazarian A., 2019. The VGT in the Circumstellar Medium around Young Stellar Objects, ApJ, 880, 148

Green D. A., 1993. A power spectrum analysis of the angular scale of Galactic neutral hydrogen emission towards L = 140 deg, B = 0 deg, MNRAS, 262, 327

HI4PI Collaboration et al., 2016. HI4PI: A full-sky H I survey based on EBHIS and GASS, A&A, 594, A116

Hall J. S., 1949. Observations of the Polarized Light from Stars, Science, 109, 166

Han J. L., 2017. Observing Interstellar and Intergalactic Magnetic Fields, ARA&A, 55, 111

Hanson D., et al., 2013. Detection of *b*-mode polarization in the cosmic microwave background with data from the south pole telescope, Phys. Rev. Lett., 111, 141301

Hartmann J., 1904. Investigations on the spectrum and orbit of delta Orionis., ApJ, 19, 268

Hartmann D., Burton W. B., 1997, Atlas of Galactic Neutral Hydrogen

Haverkorn M., 2015, Magnetic Fields in the Milky Way. p. 483, doi:10.1007/978-3-662-44625-6˙17

Hayes J. C., Norman M. L., Fiedler R. A., Bordner J. O., Li P. S., Clark S. E., ud-Doula A., Mac Low M.-M., 2006. Simulating Radiating and Magnetized Flows in Multiple Dimensions with ZEUS-MP, ApJS, 165, 188

Heiles C., Troland T. H., 2005. The Millennium Arecibo 21 Centimeter Absorption-Line Survey. IV. Statistics of Magnetic Field, Column Density, and Turbulence, ApJ, 624, 773

Hiltner W. A., 1949a. On the Presence of Polarization in the Continuous Radiation of Stars. II., ApJ, 109, 471

Hiltner W. A., 1949b. Polarization of Light from Distant Stars by Interstellar Medium, Science, 109, 165

Hoang T., Lazarian A., 2012. Spinning Dust Emission from Wobbling Grains: Important Physical Effects and Implications, Advances in Astronomy, 2012, 208159

Hu W., Dodelson S., 2002. Cosmic microwave background anisotropies, Annual Review of Astronomy and Astrophysics, 40, 171

Hu Y., Yuen K. H., Lazarian A., 2018. Improving the accuracy of magnetic field tracing by velocity gradients: principal component analysis, MNRAS, 480, 1333

Hu Y., et al., 2019a. Magnetic field morphology in interstellar clouds with the velocity gradient technique, Nature Astronomy, p. 334

Hu Y., Yuen K. H., Lazarian A., 2019b. Intensity Gradients Technique: Synergy with Velocity Gradients and Polarization Studies, ApJ, 886, 17

Ichiki K., 2014. CMB foreground: A concise review, Progress of Theoretical and Experimental Physics, 2014

Jokipii J. R., 1966. Cosmic-Ray Propagation. I. Charged Particles in a Random Magnetic Field, ApJ, 146, 480

Kalberla P. M. W., Haud U., 2015. GASS: The Parkes Galactic All-Sky Survey. Update: improved correction for instrumental effects and new data release, A&A, 578, A78

Kalberla P. M. W., Kerp J., 2009. The Hi Distribution of the Milky Way, ARA&A, 47, 27

Kalberla P. M. W., Burton W. B., Hartmann D., Arnal E. M., Bajaja E., Morras R., Pöppel W. G. L., 2005. The Leiden/Argentine/Bonn (LAB) Survey of Galactic HI. Final data release of the combined LDS and IAR surveys with improved stray-radiation corrections, A&A, 440, 775

Kalberla P. M. W., Kerp J., Haud U., Winkel B., Bekhti N. B., Flöer L., Lenz D., 2016. COLD MILKY WAY h i GAS IN FILAMENTS, The Astrophysical Journal, 821, 117

Kandel D., Lazarian A., Pogosyan D., 2016. Extending velocity channel analysis for studying turbulence anisotropies, MNRAS, 461, 1227

Kandel D., Lazarian A., Pogosyan D., 2017. Study of velocity centroids based on the theory of fluctuations in position-position-velocity space, MNRAS, 464, 3617

Kandel D., Lazarian A., Pogosyan D., 2018. Statistical properties of Galactic CMB foregrounds: dust and synchrotron, MNRAS, 478, 530

Kolb E. W., Turner M. S., 1990, The early universe. Vol. 69

Kolmogorov A., 1941. The Local Structure of Turbulence in Incompressible Viscous Fluid for Very Large Reynolds' Numbers, Akademiia Nauk SSSR Doklady, 30, 301

Koribalski B. S., et al., 2020. WALLABY – an SKA Pathfinder H i survey, Astrophysics and Space Science, 365, 118

Kovac J. M., Leitch E. M., Pryke C., Carlstrom J. E., Halverson N. W., Holzapfel W. L., 2002. Detection of polarization in the cosmic microwave background using DASI, Nature, 420, 772

Krumholz M. R., 2015. Notes on Star Formation, arXiv e-prints, p. arXiv:1511.03457

Lallement R., Vergely J. L., Valette B., Puspitarini L., Eyer L., Casagrande L., 2014. 3D maps of the local ISM from inversion of individual color excess measurements, A&A, 561, A91

Larson R. B., 1981. Turbulence and star formation in molecular clouds., MNRAS, 194, 809

Lazarian A., 2003. Magnetic Fields via Polarimetry: Progress of Grain Alignment Theory, J. Quant. Spectrosc. Radiative Transfer, 79-80, 881

Lazarian A., 2007. Tracing magnetic fields with aligned grains, J. Quant. Spectrosc. Radiative Transfer, 106, 225

Lazarian A., 2009. Obtaining Spectra of Turbulent Velocity from Observations, Space Sci. Rev., 143, 357

Lazarian A., Draine B. T., 2000. Resonance Paramagnetic Relaxation and Alignment of Small Grains, ApJ, 536, L15

Lazarian A., Finkbeiner D., 2003. Microwave emission from aligned dust, New Astron. Rev., 47, 1107

Lazarian A., Hoang T., 2007a. Radiative torques: analytical model and basic properties, MNRAS, 378, 910

Lazarian A., Hoang T., 2007b. Radiative torques: analytical model and basic properties, MNRAS, 378, 910

Lazarian A., Pogosyan D., 2000. Velocity Modification of H I Power Spectrum, ApJ, 537, 720

Lazarian A., Pogosyan D., 2004. Velocity Modification of the Power Spectrum from an Absorbing Medium, ApJ, 616, 943

Lazarian A., Pogosyan D., 2012. Statistical Description of Synchrotron Intensity Fluctuations: Studies of Astrophysical Magnetic Turbulence, ApJ, 747, 5

Lazarian A., Yuen K. H., 2018a. Tracing Magnetic Fields with Spectroscopic Channel Maps, ApJ, 853, 96

Lazarian A., Yuen K. H., 2018b. Gradients of Synchrotron Polarization: Tracing 3D Distribution of Magnetic Fields, ApJ, 865, 59

Lazarian A., Yuen K. H., Lee H., Cho J., 2017. Synchrotron Intensity Gradients as Tracers of Interstellar Magnetic Fields, ApJ, 842, 30

Lazarian A., Yuen K. H., Ho K. W., Chen J., Lazarian V., Lu Z., Yang B., Hu Y., 2018. Distribution of Velocity Gradient Orientations: Mapping Magnetization with the Velocity Gradient Technique, ApJ, 865, 46

Lu Z., Lazarian A., Pogosyan D., 2020. Producing synthetic maps of dust polarization using a velocity channel gradient technique, MNRAS, 496, 2868

Maron J., Goldreich P., 2001. Simulations of Incompressible Magnetohydrodynamic Turbulence, ApJ, 554, 1175

Mathis J. S., 1986. The Alignment of Interstellar Grains, ApJ, 308, 281

McClure-Griffiths N. M., et al., 2009. GASS: THE PARKES GALACTIC ALL-SKY SURVEY. i. SURVEY DESCRIPTION, GOALS, AND INITIAL DATA RELEASE, The Astrophysical Journal Supplement Series, 181, 398

McKee C. F., Ostriker J. P., 1977. A theory of the interstellar medium: three components regulated by supernova explosions in an inhomogeneous substrate., ApJ, 218, 148

McKee C. F., Ostriker E. C., 2007. Theory of Star Formation, ARA&A, 45, 565

Miville-Deschênes M. A., Joncas G., Falgarone E., Boulanger F., 2003. High resolution 21 cm mapping of the Ursa Major Galactic cirrus: Power spectra of the high-latitude H I gas, A&A, 411, 109

Norman M. R., 2000. Relation of neutron incommensurability to electronic structure in high-temperature superconductors, Phys. Rev. B, 61, 14751

Noutsos A., 2012. The Magnetic Field of the Milky Way from Faraday Rotation of Pulsars and Extragalactic Sources, Space Sci. Rev., 166, 307

Page L., et al., 2007. Three-year wilkinson microwave anisotropy probe (WMAP) observations: Polarization analysis, The Astrophysical Journal Supplement Series, 170, 335

Peek J. E. G., et al., 2018. The GALFA-H I Survey Data Release 2, ApJS, 234, 2

Penzias A. A., Wilson R. W., 1965. A Measurement of Excess Antenna Temperature at 4080 Mc/s., ApJ, 142, 419

Planck Collaboration et al., 2011a. Planck early results. I. The Planck mission, A&A, 536, A1

Planck Collaboration et al., 2011b. Planck early results. XX. New light on anomalous microwave emission from spinning dust grains, A&A, 536, A20

Planck Collaboration et al., 2014. Planck intermediate results. XV. A study of anomalous microwave emission in Galactic clouds, A&A, 565, A103

Planck Collaboration et al., 2015. Planck intermediate results. XIX. An overview of the polarized thermal emission from Galactic dust, A&A, 576, A104

Planck Collaboration et al., 2016a. Planck 2015 results. I. Overview of products and scientific results, A&A, 594, A1

Planck Collaboration et al., 2016b. Planck 2015 results. IX. Diffuse component separation: CMB maps, A&A, 594, A9

Planck Collaboration et al., 2016c. Planck 2015 results. X. Diffuse component separation: Foreground maps, A&A, 594, A10

Planck Collaboration et al., 2016d. Planck 2015 results. X. Diffuse component separation: Foreground maps, A&A, 594, A10

Planck Collaboration et al., 2016e. Planck 2015 results. XIII. Cosmological parameters, A&A, 594, A13

Planck Collaboration et al., 2020. Planck 2018 results. VI. Cosmological parameters, A&A, 641, A6

Pontieu B. D., Martens P. C. H., Hudson H. S., 2001. Chromospheric damping of alfven waves, The Astrophysical Journal, 558, 859

Priest E., 2014, Magnetohydrodynamics of the Sun. Cambridge University Press, doi:10.1017/CBO9781139020732

Purcell E. M., 1979. Suprathermal rotation of interstellar grains., ApJ, 231, 404

Ryden B., 2016, Introduction to Cosmology

Schlegel D. J., Finkbeiner D. P., Davis M., 1998. Maps of Dust Infrared Emission for Use in Estimation of Reddening and Cosmic Microwave Background Radiation Foregrounds, ApJ, 500, 525

Smith M. D., Mac Low M. M., 1997. The formation of C-shocks: structure and signatures., A&A, 326, 801

Smoot G. F., et al., 1992. Structure in the COBE Differential Microwave Radiometer First-Year Maps, ApJ, 396, L1

Stanimirović S., Lazarian A., 2001. Velocity and Density Spectra of the Small Magellanic Cloud, ApJ, 551, L53

Stein W., 1966. Infrared Radiation from Interstellar Grains, ApJ, 144, 318

Taylor A. R., et al., 2003. The canadian galactic plane survey, The Astronomical Journal, 125, 3145

Tonks L., Langmuir I., 1929. Oscillations in Ionized Gases, Physical Review, 33, 195

Trumpler R. J., 1930. Preliminary results on the distances, dimensions and space distribution of open star clusters, Lick Observatory Bulletin, 420, 154

Wardle M., Konigl A., 1990. A model for the magnetic field in the molecular disk at the Galactic center, ApJ, 362, 120

Xu S., Zhang B., 2016a. Interpretation of the Structure Function of Rotation Measure in the Interstellar Medium, ApJ, 824, 113

Xu S., Zhang B., 2016b. On the Origin of the Scatter Broadening of Fast Radio Burst Pulses and Astrophysical Implications, ApJ, 832, 199

Yuen K. H., Lazarian A., 2017. Tracing Interstellar Magnetic Field Using Velocity Gradient Technique: Application to Atomic Hydrogen Data, ApJ, 837, L24

Zhang K., et al., 2019. Status and perspectives of the CRAFTS extra-galactic HI survey, Science China Physics, Mechanics, and Astronomy, 62, 959506

de Bernardis P., et al., 2000. A flat Universe from high-resolution maps of the cosmic microwave background radiation, Nature, 404, 955

Appendix A

Visual Comparisons with RHT Reconstructed Maps

In this appendix we present visual comparison of the reconstructed dust polarization maps between the VChG and the RHT methods, both for the direction (Figure A.1) and the degree (Figure A.2) of reconstructed polarization. The details of maps processing and the discussion of the quantitative comparison tests can be found in the main text.
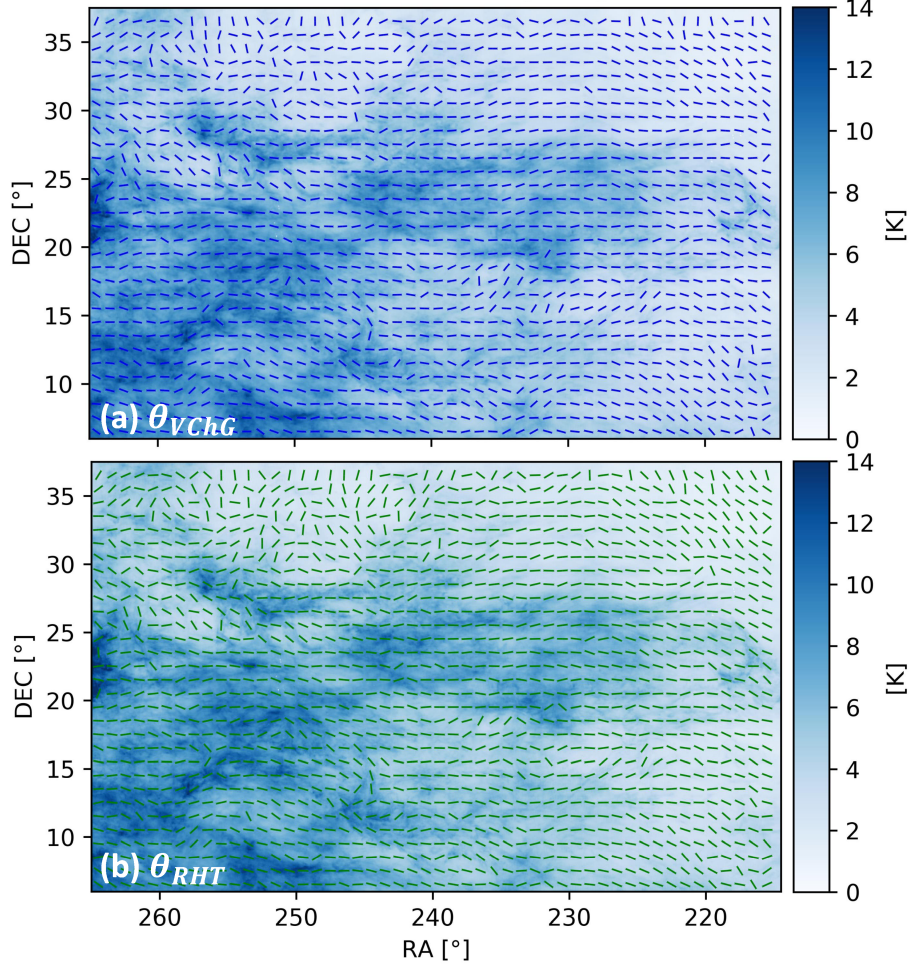
Figure A.1: Polarization direction maps of the VChGs (top panel (a)) and the RHT (bottom panel (b)). The background maps are the projected plane-of-sky intensity of GALFA-HI. The VChG is calculated from GALFA-HI data with 0.184 km/s velocity channels, ranging from -13.6 km/s to 13.6 km/s. The RHT is calculated from public RHT data with 3.68 km/s channel width, ranging from -12.9 km/s to 12.9 km/s. Both the direction maps are pixelized at 1°; the background intensity maps are pixelized at the raw resolution of GALFA-HI.
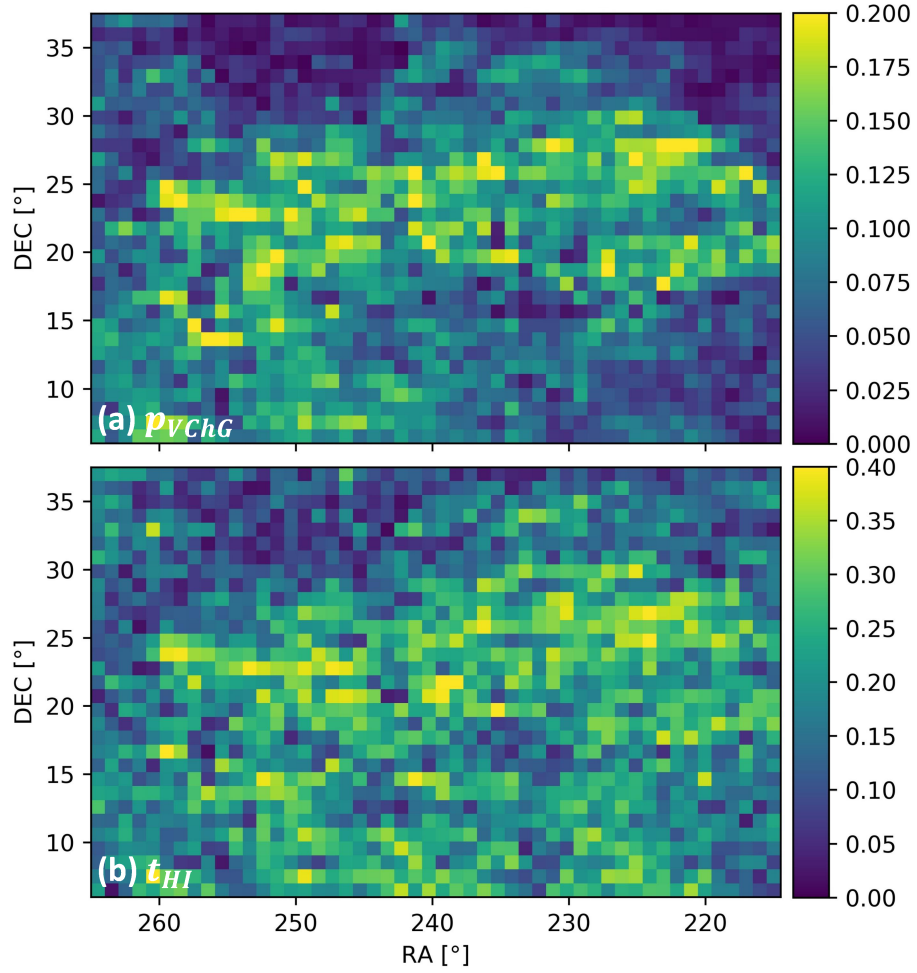
Figure A.2: Top panel (a): map of the degree of polarization p_{VChG} of the VChG. Bottom panel (b): equivalent t_{HI} parameter of the RHT method. Spatially averaged values are $\langle p_{VChG} \rangle = 0.082$ and $\langle t_{HI} \rangle = 0.19$. Both maps are pixelized at $1°$.

Appendix B

Distribution of Gradient Angle

The probability density function of two-dimensional Gaussian distribution is

$$f(x,y) = \frac{1}{2\pi(\det \boldsymbol{C})^{\frac{1}{2}}} \tag{B.1}$$

$$\times \exp\{-\frac{1}{2\det \boldsymbol{C}}[\sigma_{yy}(x-\mu_x)^2 - 2\sigma_{xy}(x-\mu_x)(y-\mu_y) + \sigma_{xx}(y-\mu_y)^2]\} \ ,$$

where the $\boldsymbol{C}$ is the covariance matrix between x and y. The determinant of $\boldsymbol{C}$ is

$$\det \boldsymbol{C} = \det\left(\begin{bmatrix} \sigma_{xx} & \sigma_{xy} \\ \sigma_{xy} & \sigma_{yy} \end{bmatrix}\right) = \sigma_{xx}\sigma_{yy} - \sigma_{xy}^2 \ . \tag{B.2}$$

In the gradient problem, x and y are the components of the gradient of the intensity field $\boldsymbol{I}(\boldsymbol{X}, v)$ in $\hat{x}$ and $\hat{y}$ direction respectively,

$$x = \nabla_x \boldsymbol{I}(\boldsymbol{X}, v) = \frac{1}{2}[\boldsymbol{I}(i+1, j, v) - \boldsymbol{I}(i-1, j, v)] \tag{B.3}$$

$$y = \nabla_y \boldsymbol{I}(\boldsymbol{X}, v) = \frac{1}{2}[\boldsymbol{I}(i, j+1, v) - \boldsymbol{I}(i, j-1, v)] \ , \tag{B.4}$$

which are both assumed to follow Gaussian distribution with zero mean value, namely, $\mu_x = \mu_y = 0$. Thus, the probability density function can be simplified

as

$$f(x, y) = \frac{1}{2\pi(\det \boldsymbol{C})^{\frac{1}{2}}} \exp\{-\frac{1}{2\det \boldsymbol{C}}[\sigma_{yy}x^2 - 2\sigma_{xy}xy + \sigma_{xx}y^2]\} . \qquad \text{(B.5)}$$

To extract anisotropy, we are interested in the probability density function of gradient angle $\theta_p = \text{atan}(y/x)$, which can be done in two steps, first to calculate the probability density function of $z = y/x$, then to calculate the probability density function of $\theta_p = \text{atan}(z)$. For the first step, the probability density function of $z = y/x$ is

$$f_{y/x}(z) = \int_{-\infty}^{\infty} |x| f(x, xz) dx \qquad \text{(B.6)}$$

$$= \int_{-\infty}^{\infty} \frac{|x|}{2\pi(\det \boldsymbol{C})^{\frac{1}{2}}} \exp\{-\frac{\sigma_{yy} - 2\sigma_{xy}z + \sigma_{xx}z^2}{2\det \boldsymbol{C}} x^2\} dx . \qquad \text{(B.7)}$$

For convenience, let us write the coefficients as

$$A = \frac{1}{2\pi(\det \boldsymbol{C})^{\frac{1}{2}}} \qquad \text{(B.8)}$$

$$B = \frac{\sigma_{yy} - 2\sigma_{xy}z + \sigma_{xx}z^2}{2\det \boldsymbol{C}} . \qquad \text{(B.9)}$$

Thus, the probability density function can be written as

$$f_{y/x}(z) = \int_{-\infty}^{\infty} A|x| e^{-Bx^2} dx \qquad \text{(B.10)}$$

$$= \int_{-\infty}^{0} A(-x) e^{-Bx^2} dx + \int_{0}^{\infty} Ax e^{-Bx^2} dx \qquad \text{(B.11)}$$

$$= \frac{A}{B} - \frac{Ae^{-B\infty^2}}{B} . \qquad \text{(B.12)}$$

Here, since

$$B = \frac{\sigma_{yy} - 2\sigma_{xy}z + \sigma_{xx}z^2}{2\det \boldsymbol{C}} \tag{B.13}$$

$$= \frac{\sigma_{xx}(z - \frac{\sigma_{xy}}{\sigma_{xx}})^2}{2(\sigma_{xx}\sigma_{yy} - \sigma_{xy}^2)} + \frac{1}{2\sigma_{xx}} \tag{B.14}$$

$$\geq 0 \ , \tag{B.15}$$

the exponential term $\frac{Ae^{-B\infty^2}}{B}$ disappears. Thus, the probability density function of $z = y/x$ can be obtained as

$$f(z) = \frac{A}{B} = \frac{(\det \boldsymbol{C})^{\frac{1}{2}}}{\pi(\sigma_{yy} - 2\sigma_{xy}z + \sigma_{xx}z^2)} \ . \tag{B.16}$$

For the second step, the probability density of gradient angle $\theta_p = \arctan(z)$ can be calculated by applying the formula

$$f_{\arctan(z)}(\theta_p) = f_z(\tan(\theta_p))(\tan(\theta_p))' \tag{B.17}$$

$$= \frac{(\sigma_{xx}\sigma_{yy} - \sigma_{xy}^2)^{\frac{1}{2}}}{\pi(\sigma_{yy} - 2\sigma_{xy}\tan\theta_p + \sigma_{xx}\tan^2\theta_p)} \frac{1}{\cos^2\theta_p} \tag{B.18}$$

$$= \frac{2}{\pi} \times \frac{(\sigma_{xx}\sigma_{yy} - \sigma_{xy}^2)^{\frac{1}{2}}}{(\sigma_{xx} + \sigma_{yy}) - \sqrt{(\sigma_{xx} - \sigma_{yy})^2 + 4\sigma_{xy}^2}\cos 2(\theta_p - \theta_B)} \ , \tag{B.19}$$

which can be simplified as

$$f(\theta_p) = \frac{1}{\pi} \times \frac{\sqrt{1 - \mathcal{J}_2}}{1 - \sqrt{\mathcal{J}_2}\cos 2(\theta_p - \theta_B)} \ . \tag{B.20}$$

The two parameters that we use for the curve fitting are

$$\mathcal{J}_2 = \frac{(\sigma_{xx} - \sigma_{yy})^2 + 4\sigma_{xy}^2}{(\sigma_{xx} + \sigma_{yy})^2} \tag{B.21}$$

$$\tan 2\theta_B = \frac{2\sigma_{xy}}{\sigma_{xx} - \sigma_{yy}} \ . \tag{B.22}$$

Note that since $z = y/x \in (-\infty, \infty)$, domain of the gradient angle $\theta_p = \text{atan}(z) \in (-\pi/2, \pi/2)$. If we consider shifting the gradient angle by $\delta\theta$, the probability density function of shifted angle, $\theta_p^* = \theta_p + \delta\theta$, will be

$$f(\theta_p^*) = f(\theta_p^* - \delta\theta)(\theta_p^* - \delta\theta)' \tag{B.23}$$

$$= \frac{1}{\pi} \times \frac{\sqrt{1 - \mathcal{J}_2}}{1 - \sqrt{\mathcal{J}_2} \cos 2(\theta_p^* - \delta\theta - \theta_B)} \;. \tag{B.24}$$

By rewriting the angle parameter as $\theta_B^* = \theta_B + \delta\theta$, the probability density function becomes

$$f(\theta_p^*) = \frac{1}{\pi} \times \frac{\sqrt{1 - \mathcal{J}_2}}{1 - \sqrt{\mathcal{J}_2} \cos 2(\theta_p^* - \theta_B^*)} \;, \tag{B.25}$$

which in form looks the same as Equation B.20. The only difference is that the domain of shifted gradient angle becomes $\theta_p^* \in (-\pi/2 + \delta\theta, \pi/2 + \delta\theta)$. This tells us that we can fit the angle histogram using the same probability density function (Equation B.20) regardless of the actual domain of the gradient angle, as long as the domain interval length is π.